



## Artificial intelligence in OCT angiography

Tristan T. Hormel<sup>a,1</sup>, Thomas S. Hwang<sup>a,1</sup>, Steven T. Bailey<sup>a,1</sup>, David J. Wilson<sup>a,1</sup>, David Huang<sup>a,1</sup>, Yali Jia<sup>a,b,\*1</sup>

<sup>a</sup> Casey Eye Institute, Oregon Health & Science University, Portland, OR, 97239, USA

<sup>b</sup> Department of Biomedical Engineering, Oregon Health & Science University, Portland, OR, 97239, USA



### ARTICLE INFO

**Keywords:**  
OCT Angiography  
Artificial intelligence  
Deep learning  
Image analysis

### ABSTRACT

Optical coherence tomographic angiography (OCTA) is a non-invasive imaging modality that provides three-dimensional, information-rich vascular images. With numerous studies demonstrating unique capabilities in biomarker quantification, diagnosis, and monitoring, OCTA technology has seen rapid adoption in research and clinical settings. The value of OCTA imaging is significantly enhanced by image analysis tools that provide rapid and accurate quantification of vascular features and pathology. Today, the most powerful image analysis methods are based on artificial intelligence (AI). While AI encompasses a large variety of techniques, machine-learning-based, and especially deep-learning-based, image analysis provides accurate measurements in a variety of contexts, including different diseases and regions of the eye. Here, we discuss the principles of both OCTA and AI that make their combination capable of answering new questions. We also review contemporary applications of AI in OCTA, which include accurate detection of pathologies such as choroidal neovascularization, precise quantification of retinal perfusion, and reliable disease diagnosis.

### 1. Introduction

Optical coherence tomographic angiography (OCTA) (An and Wang, 2008; Jia et al., 2012; Makita et al., 2006) is a novel technique that can provide microcirculatory imaging enabled by processing optical coherence tomography (OCT) data (Fujimoto and Swanson, 2016; Huang et al., 1991). The key step is quantification of speckle changes between repeated structural OCT scans, which enables the imaging of all vessels, including capillaries, through the intrinsic contrast caused by blood flow. OCTA is a functional extension of OCT, so it shares fundamental features with OCT. It's non-invasive, three-dimensional (3D), and obtains micron-scale resolution. From a clinical perspective, it's safer and faster than dye-based angiography while retaining the ability to characterize many of the same pathological features, including neovascularization (Bailey et al., 2019; de Oliveira Dias et al., 2018), ischemia (Hwang et al., 2016), and microaneurysms (Ishibazawa et al., 2015). These OCTA features and others have been shown to predict disease progression (de Oliveira Dias et al., 2018; Heiferman and Fawzi, 2019; Sun et al., 2019; Yanagi et al., 2017). This predictive capacity, as well as its non-invasive nature and ability to detect subclinical

pathologic changes (Bailey et al., 2019; Heiferman and Fawzi, 2019; Rosen et al., 2019), make OCTA procedures ideally suited for diagnostic imaging and monitoring.

These advantages largely explain the explosion of interest in OCTA research since its introduction into clinical use in 2014. A pubmed search for "OCT angiography" and "OCT + angiography" since this date yields 3670 results (as of January 2021), with over 1000 publications in 2020 alone. Despite the large volume of recent OCTA research, there is still much potential for the technology to improve. While some OCTA metrics, such as vessel density, can be provisionally estimated using simple algorithms (Corvi et al., 2018; Yang et al., 2019), even simple measurements may be inaccurate if not performed rigorously. One important reason for this is the presence of artifacts in OCTA images. As an emerging technology, OCTA data sometimes includes significant artifacts. Their severity can range from inconsequential to pervasive, even if they may appear subtle to casual inspection. Just as critically, manual grading of OCTA data can be untenable due to limited resources. This problem is especially acute for OCTA since 3D, high-resolution data requires more effort to inspect and grade. These issues must be resolved in order to validate OCTA metrics with large scale studies and enable

\* Corresponding author. Casey Eye Institute, Oregon Health & Science University, Portland, OR, 97239, USA.  
E-mail address: [jiaya@ohsu.edu](mailto:jiaya@ohsu.edu) (Y. Jia).

<sup>1</sup> Percentage of work contributed by each author in the production of the manuscript is as follows: Tristan T Hormel: 50%, Thomas S Hwang: 5%, Steven T Bailey: 5%, David J Wilson: 5%, David Huang: 5%, Yali Jia: 30%.

OCTA to reach its full potential in the clinic. Automation of OCTA analysis is therefore a priority.

Fortunately, advances in OCTA are occurring in tandem with similar improvements in image analysis driven by the introduction of artificial intelligence (AI), and in particularly deep-learning-based algorithms. AI-based algorithms are among the most important techniques in computer science, with applications across academia, commerce, and industry. At the same time, medical imaging is one of the fields that has benefitted the most from the introduction of AI, with AI-based algorithms achieving state-of-the-art performance in feature recognition and classification in several modalities, including magnetic resonance imaging (MRI), computed tomography (CT), and x-ray (Litjens et al., 2017).

AI-based analytic approaches are also well-suited for interpreting and performing measurements on OCTA data. Many AI approaches, especially those that utilize deep learning, require large quantities of data to develop. But with increasing use in clinical practice and collaborations such as the Diabetic Retinopathy Clinical Research Network (DRCR.net), the quantity of OCTA data available to researchers and clinicians is growing. Not only can we learn from the data acquired and accumulated, but we can also make full use of this data by developing reliable and accurate analytic tools.

The advanced diagnostics and quantification enabled by AI-aided analysis of OCTA data is the subject of this review, but to explain why this combination is so potent, we first discuss the general features of both OCTA imaging and AI that make the technologies complementary.

## 2. Optical coherence tomographic angiography

### 2.1. OCTA signal generation

OCT is a 3D, interferometric imaging modality that utilizes coherence gating to resolve tissue depth. It is a high resolution imaging technique, achieving capillary (approximately 10  $\mu\text{m}$ ) scale resolution with mm-scale depth penetration (Popescu et al., 2011). These parameters make the technology especially useful for examining the eye, and historically OCT has found its primary application in ophthalmic practice, although OCT also has applications in systemic disease such as

acute coronary syndrome (Arnould et al., 2018) or carotid angioplasty and stenting (Lee et al., 2019). Contemporary OCT systems achieve very high imaging speeds and efficient signal detection by using the Fourier-domain OCT principle. In Fourier-domain OCT, a spectral interferogram is obtained by combining tissue backscattering with a stationary reference reflection in an interferometer. A Fourier transform operation converts the spectral interferogram into an axial line (A-scan) that relates back-scattered reflectance to axial depth. The spectral interferogram is generated by either a rapidly tuned laser source (swept-source OCT) or a spectrometer (spectral-domain OCT). OCTA uses these high-speed OCT platforms to obtain consecutive cross-sectional images (B-scans) at the same tissue location and computes the signal alteration caused by motion (Fig. 1). Since the scans are obtained rapidly, bulk tissue motion is usually small and motion contrast is primarily generated by the motion of red blood cells in both large and small vessels, including capillaries.

Currently available OCTA algorithms vary according to the type of OCT signal used for OCTA computation, whether spectral splitting is applied to improve the flow signal-to-noise ratio, and the equations used to define the motion contrast.

As an interferometric imaging technique, the OCT signal is described by complex numbers with both amplitude (the magnitude of the real and imaginary components) and phase (the angle between the real and imaginary components), each of which change with flow related speckle variation. Consequently, the OCTA signal can be obtained by calculating motion contrast using either the amplitude, phase, or complex (i.e., containing both phase and amplitude) channel. The first successful OCTA images were captured using phase-based measurements. This is because initially attempts at obtaining angiography using structural OCT were based not on motion contrast but Doppler phase shifts (Chen et al., 1997; Izatt et al., 1997). (Doppler OCT relies on the optical analogue to the pressure/auditory phase shift familiar to us from the sound of passing sirens.) Since it seeks to measure phase shifts to determine the velocity of red blood cells and so infer blood flow speed, Doppler OCT measures phase differences between consecutive line scans. However, early experiments due to Makita et al. showed that if instead motion contrast is measured between consecutive

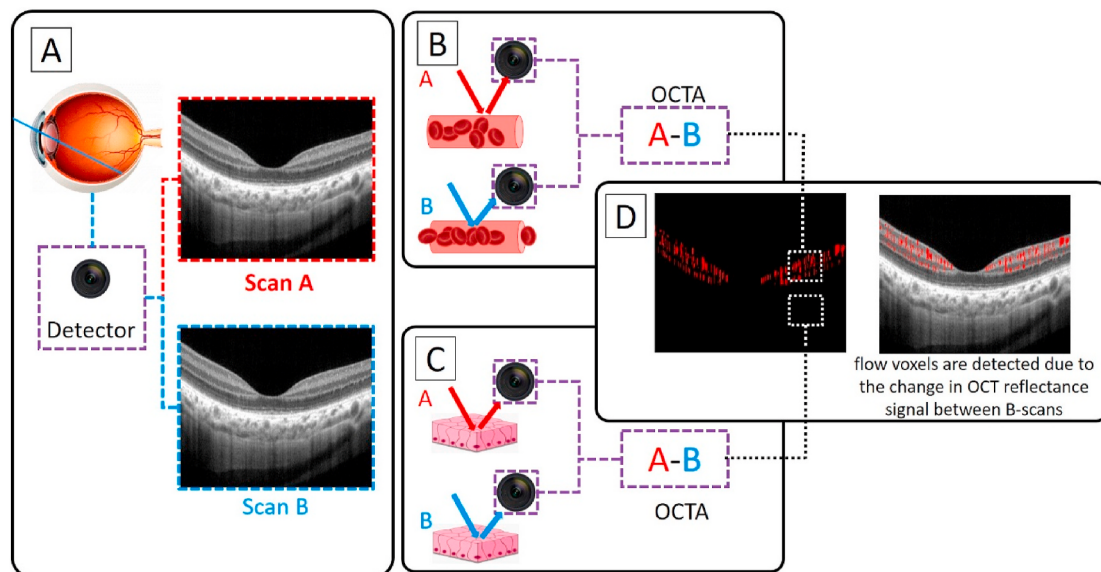


**Fig. 1.** OCTA signal generation schematic. (Panel A) An OCTA imaging procedure captures two cross-sectional structural OCT scans, scan A and scan B. (B) When the OCT sample beam encounters a blood vessel, scan A and scan B produce different signals, since the sample beam interacts with a dynamic structure. (C) On the other hand, when the sample beam encounters static tissue, the signals from scan A and scan B are identical. (D) The OCTA signal can be generated by the absolute difference between scans A and B. For beams encountering static tissue this difference is small, while for flow tissue it is large. Since it is constructed from the OCT reflectance signal, OCTA images are automatically co-registered with structural OCT images, so that the location of retinal vasculature can be readily compared to other anatomic features.

cross-sectional scans superior flow detection in capillaries can be achieved (Makita et al., 2006). Amplitude- and complex-based OCTA processing is also enabled by measuring motion contrast between cross-sectional scans (Mariampillai et al., 2008, 2010; Wang et al., 2007).

Phase-, amplitude-, and complex-based OCTA processing can all be improved by spectral splitting techniques. The most common method is to split the spectrum according to the collected frequency. Several frequency bands are then processed separately and finally averaged to form the complete image. The first split-spectrum algorithm developed for OCTA, SSADA (split-spectrum amplitude-decorrelation angiography) performed this type of spectral splitting on the amplitude signal and improved the signal-to-noise ratio for flow detection by a factor of four (Gao et al., 2015; Jia et al., 2012). The same spectral splitting in phase- and amplitude-based OCTA has also been explored (Gao et al., 2016b; Liu et al., 2016). This type of spectral splitting takes advantage of wavelength diversity to improve the signal (Pircher et al., 2003). If frequency modulation is incorporated into the OCTA device, spectral splitting can also be performed across the modulation frequency, which is linearly related to the sample beam incidence angle. The angle-resolved sub-spectrums can also be used to enhance flow detection (Li et al., 2016), which in this case boosts the flow signal through angle diversity (Wang and Rollins, 2009). It should be noted that these splitting techniques boost flow contrast by sacrificing either axial resolution (splitting along wavelength) or transverse resolution (splitting along the modulated frequency).

Most commercially available OCTA instruments rely on amplitude-based processing, since it obviates the need for phase noise compensation (as, e.g. (Makita et al., 2006; Szkulmowski et al., 2009; Wang and An, 2009; Wei et al., 2018),) required by phase- and complex-based OCTA approaches. Zeiss instruments, however, use the complex-signal-based optical microangiography (OMAG) processing method (An et al., 2011). The advantage of complex-based processing is that it uses all the information theoretically available in an OCTA scan; OMAG is consequently an efficient algorithm, requiring only two repeat cross-sectional scans per imaging plane to produce an OCTA volume.

Due to spectral splitting, SSADA is a similarly efficient algorithm, also capable of detecting flow in capillaries from just two repeated cross-sectional scans. SSADA is commercialized in Optovue instruments. Other commercialized approaches are, like SSADA, amplitude-based, but they rely on sampling a larger number of cross-sectional scans to differentiate vascular and static tissue. Heidelberg instruments measure the temporal amplitude distribution within a given voxel, which yields high contrast images and requires four to seven B-scans to adequately sample these amplitude distributions (Rocholz et al., 2018). In Topcon instruments, the ratio between the maximum and minimum amplitude in cross-sectional frames is measured; this method (OCTA ratio analysis, OCTARA) also requires at least four consecutive scans to achieve OCTA (Yang et al., 2010). There are also many other variations on OCTA processing that have been published in the literature but are not currently available in commercial instruments, for example (Li et al., 2016; Liu et al., 2014, 2016; Schwartz et al., 2014; Wei et al., 2018; Xu et al., 2016).

With increasing system speeds and sensitivities, it may also soon be possible to visualize some capillary networks using structural OCT. However, the superficial vascular complex resides in high reflectance tissue, which would make such visualization difficult. It is likely that viewing this structure will continue to require OCTA, and the ability to discriminate vessels by measuring flow will similarly remain useful as OCT systems improve.

## 2.2. OCTA visualization

Since it procures three-dimensional data, there are multiple ways to visualize OCTA (Fig. 2). *En face* images are the most frequently used OCTA representation. They are analogous to the images procured by fluorescein and indocyanine green angiography, and so are the most natural way to compare with these modalities. Furthermore, many common OCTA metrics, such as vessel density, are usually measured from *en face* images (Corvi et al., 2018; Rabiolo et al., 2018; Yang et al., 2019).

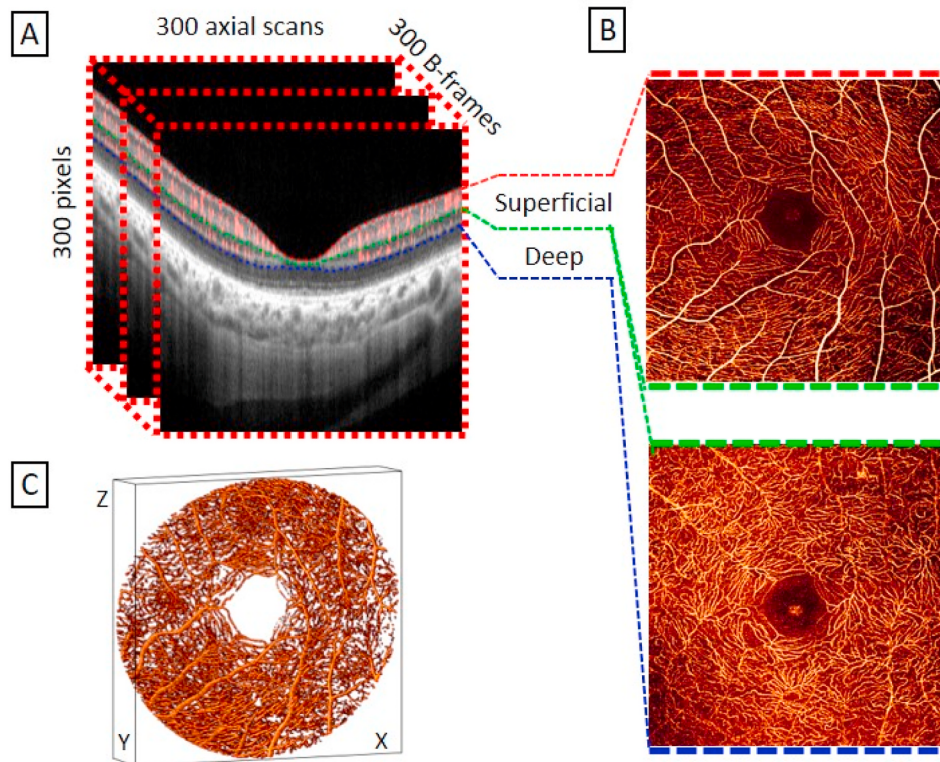


**Fig. 2.** OCTA data representations. (A) Cross-sectional images can be generated from individual B-frames, or by projecting several B-frames to form a composite image. In the example images here, three anatomic slab boundaries are colored red, green, and blue. (B) The flow signal can be projected between these boundaries to create *en face* representations, which are akin to color fundus photography and dye-injection angiography images. (C) Since OCTA is a three-dimensional imaging modality, volume renderings can also be used.

OCTA data is amenable to *en face* representations due to the orientation of the retinal plexuses. The retina includes four plexuses: the nerve fiber layer plexus (NFLP), ganglion cell layer plexus (GCLP), intermediate capillary plexus (ICP), and deep capillary plexus (DCP). These plexuses can be grouped into complexes, with the NFLP and GCLP forming the superficial vascular complex (SVC) and the ICP and DCP forming the deep vascular complex (DVC). Any of these plexuses or complexes are good targets for producing *en face* images, since pathology may be present in only a single plexus or complex, or may manifest differently in individual plexuses even when it is involved in multiple (Hormel et al., 2020; Patel et al., 2018). Images of plexuses or complexes in isolation can be achieved by projecting flow signal within a retinal slab on to a plane. There are several ways this projection can be performed; within the retina, maximum-value projection achieves the highest signal-to-noise ratio and contrast (Hormel et al., 2018). Slabs over which flow signal is projected are usually defined in terms of physiological retinal layers that can be distinguished using the structural OCT signal. Because of the need to produce *en face* images of plexuses or complexes, retinal slab segmentation is a basic step in OCTA interpretation and analysis. We will return to this topic below, since state-of-the-art layer segmentation algorithms rely on artificial intelligence. With proper projection, *en face* images can greatly improve identification and assessment of some pathologies (Fig. 3).

Cross-sectional scans are the other common OCTA representation. Cross-sectional scans are frequently used in structural OCT in order to detect pathology such as edema (through identification of either fluid pockets or abnormal thickening of the retina), detachments, or disorganization of retinal layers (Browning et al., 2008; Das et al., 2018; Prager et al., 2014; Sun et al., 2015). Fewer features are measured using cross-sectional OCTA due to the orientation of retinal vascular plexuses (Campbell et al., 2017). But some important vascular pathologic

developments do show a strong signal in cross-sectional scans (Patel et al., 2018). A good example is retinal angiomatic proliferation, in which neovascular growth between the retina and choroid can be directly imaged (Bhavsar et al., 2017) (Fig. 3). Since information in cross-sectional images is projected along B-frames instead of anatomic layers, a final advantage for this representation is that it does not require slab segmentation. For this reason, it can be helpful to review cross-sectional scans in order to confirm that vessels that may appear to be neovascular are not simply mis-segmented into the wrong retinal slab.

The three-dimensionality of OCTA data can also be leveraged to produce volume renderings (Fig. 4). Volume renderings have the advantage of allowing simultaneous inspection of lateral and vertical position, but they are often less straightforward to interpret. Furthermore, they must obscure features in the rear of the image to provide clarity to features in the fore. Nonetheless, they can avoid some distortions that can occur in projected representations (Guo et al., 2020), and can help to determine the location of pathology such as cystoid macular edema with respect to vascular defects (Spaide, 2016).

### 2.3. OCTA artifacts

In addition to flow signal attributable to blood within vessels, OCTA data may also contain artifacts. Artifacts are relatively common in OCTA data, with one study finding at least a single artifact of any type in 98% of the images analyzed (Holmen et al., 2019). The good news is that many of these artifacts will not seriously degrade image quality. Furthermore, contemporary algorithms, such as e.g. (Camino et al., 2017; Wang et al., 2017), can suppress many of the most detrimental types of artifacts. Nonetheless, the presence of artifacts within OCTA data remains one of the driving requirements for incorporating artificial

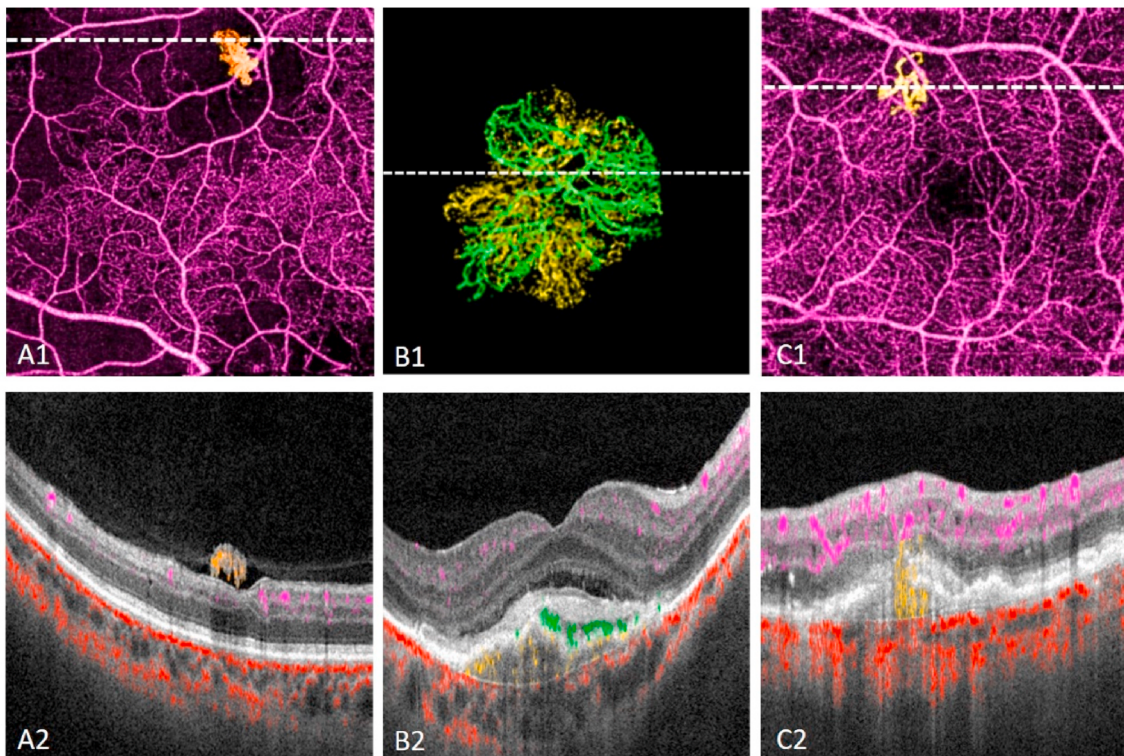


**Fig. 3.** *En face* and cross-sectional OCTA representations highlighting retinal neovascularization (RNV), choroidal neovascularization (CNV), and retinal angiomatic proliferation (RAP). In each image, the flow signal is color coded according to its position (orange: vitreous; violet: inner retina; yellow: outer retina, red: choroid). (A) The RNV lesion can be clearly located in the *en face* and cross-sectional images due to its location in the vitreous. (B) Here, the outer retinal vessels are additionally colored according to location relative to the retinal pigment epithelium (green: above, yellow: below). This enables easy identification of type 1 (yellow) and type 2 (green) CNV, and can help identify mixed lesions such as the example here. (C) A cross-sectional view clearly shows the RAP vessels extending between the choroid and outer retina. In all of the examples shown, both the *en face* and cross-sectional images can help to identify and characterize the pathology.

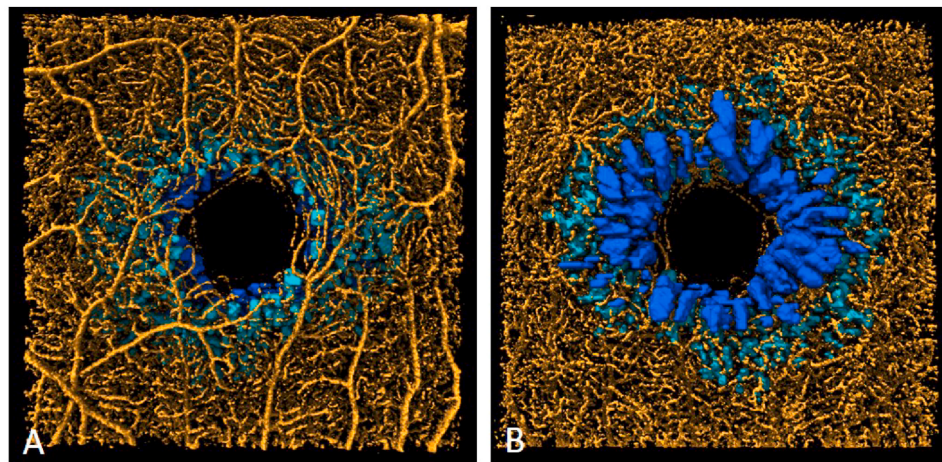


**Fig. 4.** Volume renderings of an eye with a macular hole. (A) View looking down from the superficial vascular complex, and (B) looking up from the deep capillary plexus. Blue indicates intra-retinal cystoid spaces, with light blue indicating a location in the inner nuclear layer and dark blue between the outer plexiform layer and Henle's fiber layer. Volumetric representations can avoid misleading images in which extended fluid volumes may appear small due to their projected area in cross-sectional or *en face* images.

intelligence into algorithm design, since deep-learning-based algorithms can often compensate for residual artifacts.

### 2.3.1. Projection artifacts

Depth resolution in OCTA is obtained through coherence gating, which maps the optical path length traveled by a detected photon to an anatomic location in the retina. For a photon reflected by a single scattering event, this optical path length is just the round trip distance to the scatterer. However, according to Mie scattering theory and simulations (Karlsson et al., 2005; Lu et al., 2005), photons are frequently forward-scattered by blood cells. Such photons acquire time-varying phase and amplitude changes due to blood cell motion. If they are subsequently backscattered by static tissue and detected they will map motion contrast to the depth of their total path length, not the path length to the blood cells that imparted the amplitude or phase changes. This results in projection artifacts: measurable motion contrast signal emanating from static tissue posterior to vessels. In *en face* images projection artifacts mimic the appearance of superficial vessels, while in cross-section they produce extended tails that cause vessels to appear elongated (Fig. 5).

Projection artifacts can have large effects on OCTA interpretation and quantification. In part this is because they can be readily confused

for real vessels in *en face* images due to their similar appearance. Projection artifacts are also ubiquitous, and will be present in any OCTA images unless they are removed in postprocessing. The combination of these features (vascular appearance and frequency of occurrence) are probably the reason that many early OCTA studies distinguished only a superficial and a deep plexus (Agemy et al., 2015; Savastano et al., 2015; Spaide et al., 2015) instead the anatomically correct four (Campbell et al., 2017). Projection artifacts are also extremely disruptive to detection and quantification of choroidal neovascularization. The outer retina is avascular in healthy eyes, so the presence of vessels there could be readily identified as pathology-except that projection artifacts produce false flow signal in the outer retina (Fig. 5 E1). Projection artifacts in the outer retina can both be mistaken for true neovascularization when it is absent and disguise neovascularization when it is present (Dansingani et al., 2015). Projection artifacts also hinder the quantification of other vascular features in deeper plexuses. For example, vessel density measurements made on the intermediate or deep capillary plexus without projection artifact removal-as in (Chidambara et al., 2016; Lei et al., 2017a; Wang et al., 2016)- produce measurements that blend information from both superficial and deep vasculature to produce composite densities.

The literature contains references to two important artifact removal

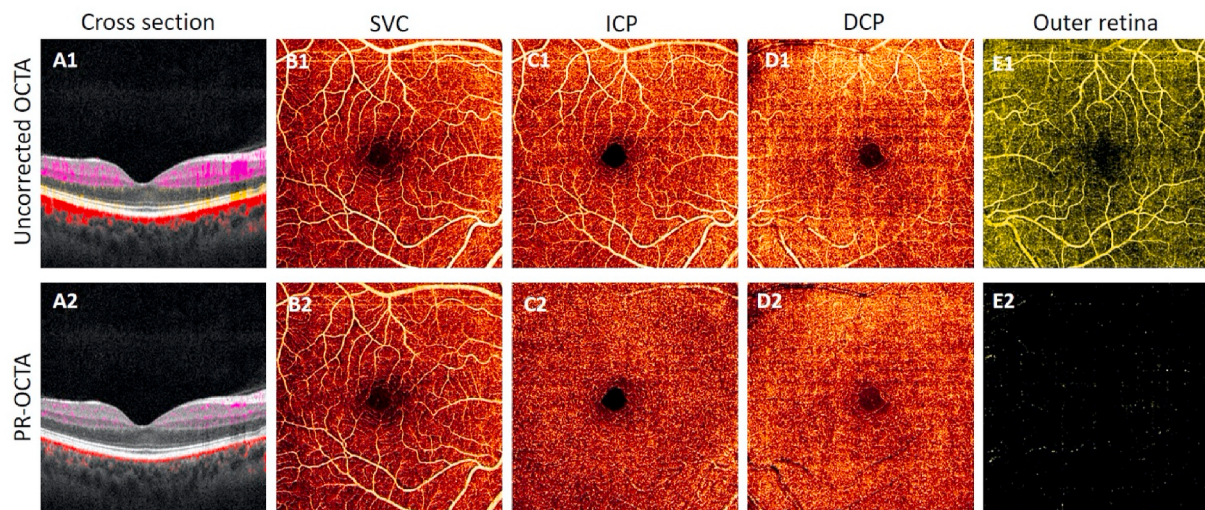


**Fig. 5.** Projection artifacts and their removal from 6 × 6-mm OCTA images. (Top row) Uncorrected OCTA data includes projection artifacts in both cross-sectional and *en face* images. (A1) In cross-section, projection artifacts manifest as tails extending below vessels. In this image, the flow signal is overlaid on the structural image (gray scale), and colored according to anatomic depth (violet: inner retina, yellow: outer retina, red: choroid). In *en face* images, the flow signal from the superficial vascular complex (SVC; B1) is duplicated in the intermediate capillary plexus (ICP; C1), deep capillary plexus (DCP; D1) and the outer retina (E1), which is avascular in healthy eyes. (Bottom row) Projection-resolved OCTA (PR-OCTA) removes projection artifacts in both cross-sectional and *en face* images.

techniques: slab subtraction and projection-resolved OCTA (PR-OCTA). Slab subtraction was proposed first, and consists of subtracting the weighted flow signal in superficial *en face* images from *en face* images produced in deeper anatomic slabs (Jia et al., 2015; 2014a; A. Zhang et al., 2015). This approach has the advantage of unambiguously removing false flow signal. But it is also a heavy-handed approach that results in fragmentation of vascular networks since any real flow signal co-occurring with projection artifacts will also be removed. Furthermore, since slab subtraction is performed on *en face* images, it does nothing to eliminate the vessel tails seen in cross section.

This is in contrast to PR-OCTA (Wang et al., 2017; Zhang et al., 2016a), which operates volumetrically and so is equally capable of removing projection artifacts from cross-sectional and *en face* images (Fig. 5). Instead of subtracting the flow signal in superficial layers, PR-OCTA weights the OCTA signal in deeper layers using information from reflectance images and superficial flow. The resulting cross-sectional images do not show artifactual tails descending from vessels, and *en face* images are cleaned without the severe vessel disruptions produced by slab subtraction. Despite this, residual projection artifacts are still present more often in PR-OCTA than in slab subtracted data. Of course, the approaches are not mutually exclusive, and slab subtraction can be used to identify residual projection artifacts in PR-OCTA *en face* images (Wang et al., 2020a).

### 2.3.2. Shadowing artifacts

Where projection artifacts introduce false flow signal, shadow artifacts remove true flow signal (Fig. 6). Shadowing artifacts are caused by OCT signal attenuation. This signal attenuation can be due to pathology within the retina such as drusen, hyperreflective foci, or retinal detachments. But even in healthy eyes shadowing can occur beneath large vessels. Shadowing may also be due to features outside the retina, for example vitreous floaters, cataract, or hemorrhage. Another major source of shadowing is vignetting, which can occur when either the

OCTA device is misaligned or imaging is occurring at more peripheral locations that may be affected by the pupil aperture (Wei et al., 2019).

Similar to projection artifacts manifesting as apparent neovascularization, shadowing artifacts can also mimic the appearance of real pathology such as capillary dropout. Shadowing artifacts can consequently significantly impinge on any ischemia-related measurements, such as vessel density and nonperfusion area. Shadowing artifacts can also disguise other pathologic developments, for example by blotting out a region where neovascularization occurs.

Shadowing artifacts can be strong enough that they prevent recovery of the OCTA flow signal. This means that, unlike many OCTA artifacts, severe shadows cannot always be suppressed or compensated for. Instead, severe shadowing-artifact-affected regions should be identified and precluded from quantitative analysis. Because the interplay between the various features that can identify shadowing artifacts is complex, shadowing artifact detection algorithms have tended to rely on machine learning, and we will return to these approaches later.

### 2.3.3. Other OCTA artifacts

Motion artifacts are generated by any movement in the eye not attributable to blood flow. Such motion includes microsaccadic movements. Microsaccades manifest as bright strips in OCTA images, and they may also cause doubling of anatomic features if the eye shifts from the fixation target (Fig. 7). Microsaccadic artifacts can usually be removed by registering data from two orthogonal fast scanning directions (often called x-fast and y-fast scans) (Camino et al., 2016a; Hendargo et al., 2013; Kraus et al., 2012, 2014). Another approach is to use parallel strip registration with multiple scans along the same priority axis (Zang et al., 2016, 2017b).

Other sources of motion artifacts include ocular pulsation and drift. These eye movements are much slower than microsaccades, and consequently the motion artifacts they generate are not as prominent as microsaccadic artifacts, appearing instead as a heightened background

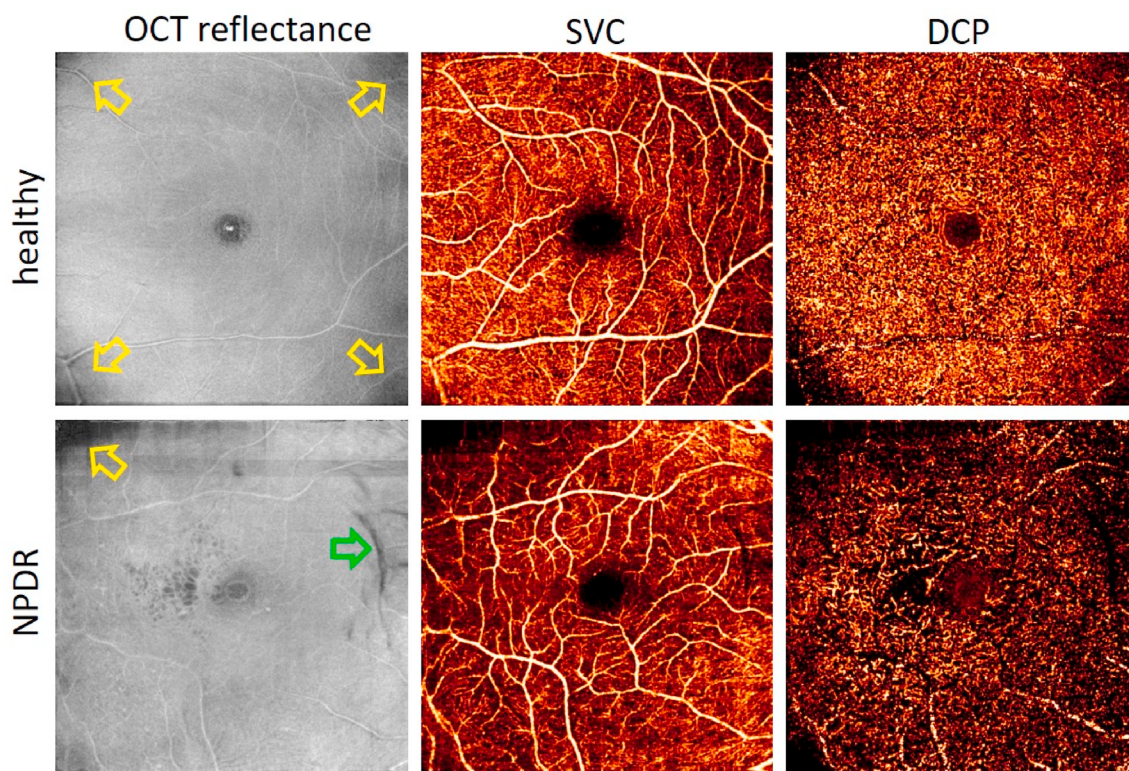


**Fig. 6.** Shadowing artifacts. *En face* images of a healthy volunteer (top row) shows shadows caused by vignetting (yellow arrows) in the OCT reflectance channel (left column), superficial vascular complex (SVC), and deep capillary plexus (DCP). The shadowing artifacts are more prominent in the deeper layers. Vignetting as well as a shadow due to a vitreous floater (green arrow) are apparent in an eye with non-proliferative diabetic retinopathy (NPDR; bottom row).

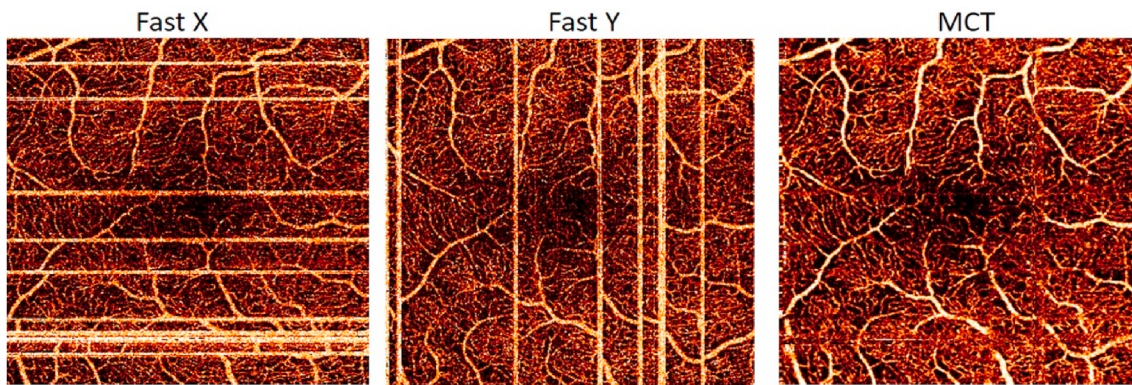


**Fig. 7.** Microsaccadic artifacts and their removal. Scanning along a priority axis will produce Fast X and Fast Y scans, in which microsaccades manifest as bright lines in the scanning direction. These artifacts can be corrected by registering and merging the images, as shown in the motion correction technology (MCT) image. However, note some residual artifacts still present in the MCT image.

level. In severe cases motion artifacts could cause thresholding errors, but even in less severe cases they can make vascular patterns less pronounced.

Motion artifacts can also be prevented using hardware-based motion control systems. These systems typically rely on auxiliary imaging technologies (for example, scanning laser ophthalmoscopy or video camera) in order to either track eye movements or trigger re-scans if eye motion is too swift (Braaf et al., 2013; Camino et al., 2016b; Ferguson et al., 2004; Vienola et al., 2012; Zang et al., 2016; Q. Zhang et al., 2015). A disadvantage of such approaches is that capillaries may not be visible using the allied modalities, which could cause them to be mis-registered. Incorporating other imaging systems into OCTA devices will also increase the cost of the system. Motion control systems that rely on graphics processing unit (GPU)-based real-time OCTA can eliminate these concerns (Wei et al., 2020a). In addition to these hardware-based approaches, motion artifacts can also be removed with AI-based image processing, as discussed below.

Signal strength reduction can also lead to errors in quantifying OCTA data. Defocusing caused by instrument misalignment is one source of signal strength reduction. Defocusing results in a lower signal strength, leading to a smaller signal-to-noise ratio. Defocusing also broadens vessel caliber while reducing vessel contrast. Signal strength is also affected by intrinsic features of the eye being imaged, such as media opacity. Signal strength in OCTA images correlates with vessel density measurements (Yu et al., 2019) and influences other OCTA metrics as well, which can stymie efforts to diagnose and monitor diseases. Signal strength effects could be eliminated by calibrating the linear effect between signal strength and vessel density measurement (Gao et al., 2016a), but this would require collecting sufficient data for each instrument and would not eliminate effects due to defocusing. Traditional image filtering, for example with Gabor, Gaussian, or Frangi filters can help to accentuate vasculature while suppressing background (Chlebiej et al., 2019; Frangi et al., 1998; Tan et al., 2018). Contemporary machine-learning-based image enhancement can also be used to highlight vasculature.

A final noteworthy source of artifacts in OCTA are segmentation artifacts, which occur when anatomic slabs are mis-segmented, causing features from one anatomic region to be incorrectly mapped to another. This could lead to normal vessels appearing as neovascularization if they are mis-segmented into avascular tissues. Segmentation artifacts can be corrected by careful inspection of cross-sectional scans. However, this process is laborious and it may be impractical to review a large number of cross-sectional scans in clinical practice. A better solution is improved automation of slab boundary detection. This is a problem that is also well-suited to artificial intelligence, a subject to which we now turn.

### 3. Artificial intelligence

Artificial intelligence (AI) encompasses a broad class of techniques in computer science that can reliably perform human cognitive tasks (Russel and Norvig, 2020) (Table 1). Here, we cover just a few salient points that will help with understanding the use of AI in OCTA analysis. Colloquially AI is sometimes used synonymously with the term “machine learning”, but AI need not rely exclusively on learning-based approaches. For example, one of the first AI-based treatment recommendation systems, MYCIN, was a knowledge base system that output treatment recommendations based on a list of explicitly coded rules (Buchanan and Shortliffe, 1984).

Nonetheless, AI accomplishments that have captured the popular imagination are largely achievements of learning-based approaches (Brown and Sandholm, 2019; Nassif et al., 2019; Silver et al., 2016). Part of the reason is that learning-based algorithms demonstrate a clear superiority in tasks that defy concise formal description, and are instead highly complex or “intuitive” in some sense. For example, identifying foreground and background objects in an image based only on intensity can be formally described as the selection of an intelligent threshold value (Otsu, 1979). This procedure, however, only demarcates bright and dark regions within an image, which are not in general equivalent to the complex image features we usually want to quantify in medical imaging (Litjens et al., 2017).

Many state-of-the-art algorithms in ophthalmology (Schmidt-Erfurth et al., 2018; Ting et al., 2018) and beyond (Shen et al., 2017) are deep-learning-based. Deep learning algorithms can be distinguished from shallow learning algorithms by the presence of hidden layers between the algorithm input and output (Bishop, 1995). These hidden layers allow deep-learning-based models to encode a more complex feature space in order to solve abstract problems like semantic segmentation. Deep learning networks are able to do this by training from

**Table 1**

Artificial intelligence methods. AI is an enormous field that encompasses many techniques. The image at left shows deep learning as a subfield within machine learning, which is also a subfield of AI.

Technology	Example methods
Artificial intelligence	Principle component analysis
Machine learning	Machine learning
Deep learning	Support vector machines Random forest Regression Deep learning Convolutional neural networks Recurrent neural networks

data.

### 3.1. Training and evaluation

Learning-based algorithms require data to tune parameters and perform effectively. Usually the majority of the data in machine learning development is used for training, as either training or validation data sets, with the remainder comprising the test dataset. Training data is used to adjust model parameters to optimize an objective function (Fig. 8). This procedure guarantees the model will perform well on the training data, but does not guarantee it will generalize to data it has never encountered. To improve generalizability, some data may also be reserved for validation. Validation data is seen during the training process, but not used in the gradient calculations that update learned parameters (Le et al., 2011). Instead, at the end of a training epoch (i.e. a single pass through the training data set), the model analyzes the validation data set in order to assess generalizability.

Data not used during training can be used for testing (Fig. 8). Assessing learning-based algorithms on testing data is necessary to gauge the generalizability of the model. For algorithm performance assessment to be fair, the data used in training and testing should be mutually exclusive. For OCTA, this means that test data and training data should be drawn from different individuals.

Model performance on test data may deteriorate while still improving on training data. This issue, overfitting, is a significant problem in machine learning that is more acute with the limited data set sizes encountered in OCTA. (By way of comparison, learning-based algorithms trained on ImageNet, a popular labeled public data set, have millions of examples to learn from (Deng et al., 2009), while OCTA data sets may be limited to only hundreds of *en face* images for algorithms targeting some pathologies, as e.g. in (Wang et al., 2020a)). In such situations researchers can appeal to data augmentation strategies, such as image rotations, reflections, and translations, or more complex data

transformations, in order to bolster the size of the training data set (Shorten and Khoshgoftaar, 2019).

Objective functions, also called loss functions, measure the error associated with parameter values in machine learning models. As such, they are task-specific. For example, categorical cross-entropy is often employed in classification tasks, but constructions such as a structural similarity index may be more appropriate for image reconstruction (as in e.g. (Gao et al., 2020)). Like model inputs and outputs, the choice of a loss function is a design feature that influences algorithm performance (Janocha and Czarnecki, 2017).

### 3.2. Ground truth label generation

Machine learning approaches are often characterized as supervised or unsupervised, although the distinction between the two is not always clear cut, and other paradigms, such as reinforcement learning, also exist. In unsupervised learning, algorithms are designed to learn features latent within data sets. Examples relevant for OCTA include image denoising algorithms, in which algorithms can attempt to learn features that generate the image in order to suppress noise. Another example is data clustering, in which latent features are used to sort data into categories.

Supervised learning approaches are more common in OCTA. These approaches require ground truth labels for training, and algorithms are designed to predict a label from input data. Pixel-wise segmentation and image classification are examples of tasks normally accomplished using supervised learning.

Ground truth label generation represents a problem specific for supervised learning techniques. Inter-observer variability should be considered when generating ground truth labels for clinical data. Even experienced graders will sometimes place the same OCTA data into different categories (Woetzel et al., 2019). This issue is exacerbated when we attempt to generate pixel scale ground truths, since at this scale

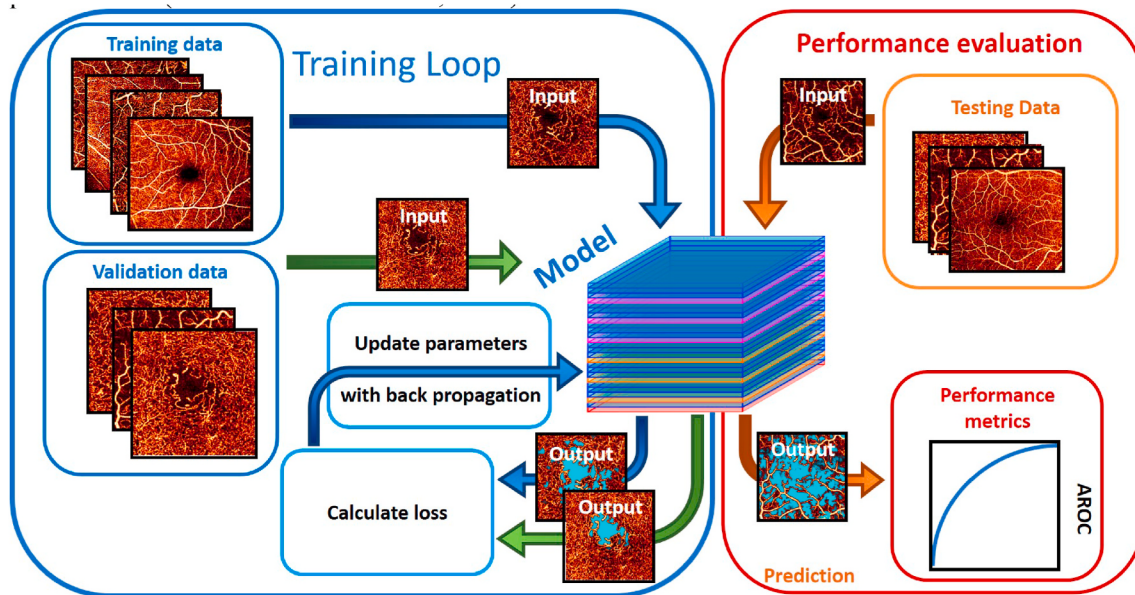


**Fig. 8.** Training and evaluation in machine learning (schematic). The goal of a learning algorithm (portrayed as a convolutional neural network labeled “model”, above) is to achieve adequate performance on previously unseen data in a specific task by learning from a training data set. Here, an example of training a network to segment non-perfusion area in an OCTA *en face* image is shown. During training (training loop panel above) the training data is input to the model (blue arrows). The model’s output on the training data is compared to a benchmark or ground truth, with its performance evaluated by means of a loss function. By updating parameter values to minimize the loss, the network can learn features in the data and improve its performance on the training data. Most networks can achieve reliable results on training data, but the real question is if the network can generalize to perform the same task on unseen data, like images of a new patient. To assess generalizability a validation data set is often also included in the training data (green arrows). The validation set is characterized during the training process the same as the training data, but the results are not used in parameter updates. In this way generalizability can be gauged during training, since the model does not learn the validation set. To fully assess generalizability, a unique testing data set is used (performance evaluation panel; orange arrows). Here, the network’s performance is evaluated with metrics like the area under receiver operating characteristic curve (AROC).

different graders will essentially always disagree on the category of some individual pixels. The result is that graders can sometimes share only moderate agreement for some OCTA quantifications, for example CNV membrane area (Leal et al., 2020). Since supervised learning algorithms must learn from these labels, any mislabeling will cause the algorithm to also learn to mislabel the feature. When possible, it is best to generate durable ground truth labels by incorporating review from multiple graders or, in the case of pixel-wise labeling, using multiple graders and determining the final ground truth labels based on the majority.

The existence of inter-observer variability is another reason to attempt automated, end-to-end OCTA quantification, since high performance algorithms can eliminate some of the tacit, subjective decisions that prevent grader agreement.

### 3.3. Convolutional neural networks

Another major consideration when designing a machine learning model is the network architecture. Contemporary state-of-the-art image analysis network are deep learning architectures called convolutional neural networks (CNNs) (Rawat and Wang, 2017). CNN architectures often encountered in image analysis tasks relevant to OCTA analysis are given in Table 2. Considering the subject matter of this journal, it is interesting to note that CNN architectures drew inspiration from hierarchical models (DiCarlo et al., 2012; Fukushima, 1980) that attempted to explain pioneering experiments recording the stimulus response of individual neurons in the cat and macaque visual systems (Hubel and Wiesel, 1959, 1968). In these models, neurons are excited or inhibited by stimulus within only a limited receptive field, a concept that is incorporated into CNN architectures through the use of the convolution operation. Hierarchical models also distinguish two types of neurons in the primary visual cortex: simple cells, which respond to stimulus at a particular location, orientation, and phase (that is, they would not respond to a black/white inverted image), and complex cells, which have larger receptive fields and tolerate changes in position and phase. The congruence between some features learned by the first hidden layers in CNNs and features that activate simple cells—namely Gabor-filter-like responses—indicates that CNNs function in a way that is at least consistent with some aspects of mammalian visual processing (Hyvärinen et al., 2009). Finally, in hierarchical models visual stimulus is processed sequentially in the retina, then the lateral geniculate nucleus of the thalamus, and finally to the primary visual cortex, extrastriate visual areas V2 and V4, and the inferotemporal cortex. Similarly, CNNs are also feedforward networks. Outside of this connection to mammalian visual processing, CNNs are still worthy of special consideration because they consistently outperform other image analysis network architectures by wide margins, and have been doing since the introduction of AlexNet in 2012 (Krizhevsky et al., 2012).

Convolutional neural networks are distinguished by their reliance on convolution operations. These operations use an input (e.g. an image or feature map from a hidden layer) and a convolution kernel with trained values to produce an output feature map. Convolution operations have several advantages over matrix multiplication, or fully connected layers. They are sparsely connected. This makes them orders of magnitude more computationally efficient than fully connected layers because the convolution kernel only connects inputs within an output's receptive field, rather than the entire input data. This property makes CNNs feasible to train. This property also exploits the notion that much of the information latent in an image is inherently local. For example, the foveal avascular zone well always occur in a single location within an OCTA image, rather than within several disconnected regions. CNNs also employ weight sharing. This means that the same kernel is applied sequentially across the entire image, which does not reduce computational complexity but does reduce memory costs. Furthermore, since the same kernel is applied to the entire feature map or input image, a small shift in the input, such as moving an entire image a pixel to the right, will

not drastically change output (Goodfellow et al., 2016).

Convolution layers in CNNs are usually paired with activation layers, which in state-of-the-art networks consist of rectified linear units (ReLUs), and pooling layers. Activation layers introduce non-linearities that help with network generalization (Jarrett et al., 2009). The most common type of pooling layer is a max-pooling layer, which replaces a grid value with the largest value in its receptive field. Pooling layers can also help improve model generalizability when used to downsample an image or feature map, in which case they can ensure the translation invariance of the model output. CNNs can also learn other invariances (e.g. rotational or scale invariance) (Goodfellow et al., 2016). These properties are important since in OCTA we usually want to detect pathologic features independent of location, size, or orientation.

Convolution, activation, and pooling layers are just three of the most important constructions in CNNs. There are many other components and variations that can be included. As an example of a CNN, we can consider a simple U-net-like model (Fig. 9). U-nets consist of an encoder arm, which learns representations of features, and a decoder arm, which translates these features back into pixels in the output image. This general structure is common to all encoder-decoder networks, which form the basis of many image segmentation CNNs. The U-net improves performance by including skip connections between the encoder and decoder arms, which help to maintain the resolution of the output (Ronneberger et al., 2015). Skip connections are also used by resnet modules (He et al., 2016), which form the basis of many state-of-art classification algorithms (Fig. 10). The advantage of this architecture is that it allows construction of very deep networks that can include over a hundred hidden layers. Such deep networks have the capacity to learn complex features, but are more difficult to train. Resnet modules are helpful in this regard.

### 3.4. Other artificial intelligence algorithms

We include a discussion of CNNs because they have found widespread use in contemporary image analysis. However many other artificial intelligence algorithms are also useful and still often employed. For example, regression-based approaches (Wang et al., 2010), principle component analysis (Jolliffe, 2002), data clustering (Ester et al., 1996), support vector machines (Suykens and Vandewalle, 1999), and many other approaches can all be used to characterize images and extract measurements. Discussion of each of these approaches is beyond the scope of this review; interested readers are referred to (Klette, 2014).

## 4. Artificial intelligence in OCTA

The previous sections discussed basic principles of OCTA data acquisition, generation, and processing, and AI-aided image analysis. Now we will discuss the pairing of these technologies. Artificial intelligence is well situated to take advantage of the large quantities of detailed information procured by OCTA. The most powerful techniques in artificial intelligence are machine-learning-based, and each OCTA data volume can be resampled to create hundreds of images (for example, by considering each B-frame separately). This indicates the feasibility of using AI for OCTA analysis. On the other hand, many image analysis tasks in OCTA call for intelligent algorithms. OCTA images frequently include artifacts that are difficult to remove with handcrafted algorithms. Furthermore, many of the pathologies we would like to quantify produce complicated signals themselves. These signals are not always amenable to analysis by handcrafted algorithms.

### 4.1. Making OCTA images with AI

#### 4.1.1. OCTA signal generation

Signal generation in OCTA data calls for the acquisition of multiple B-scans in order to measure motion contrast and extract flow signal. As an alternative, learning algorithms can be taught to create OCTA-like

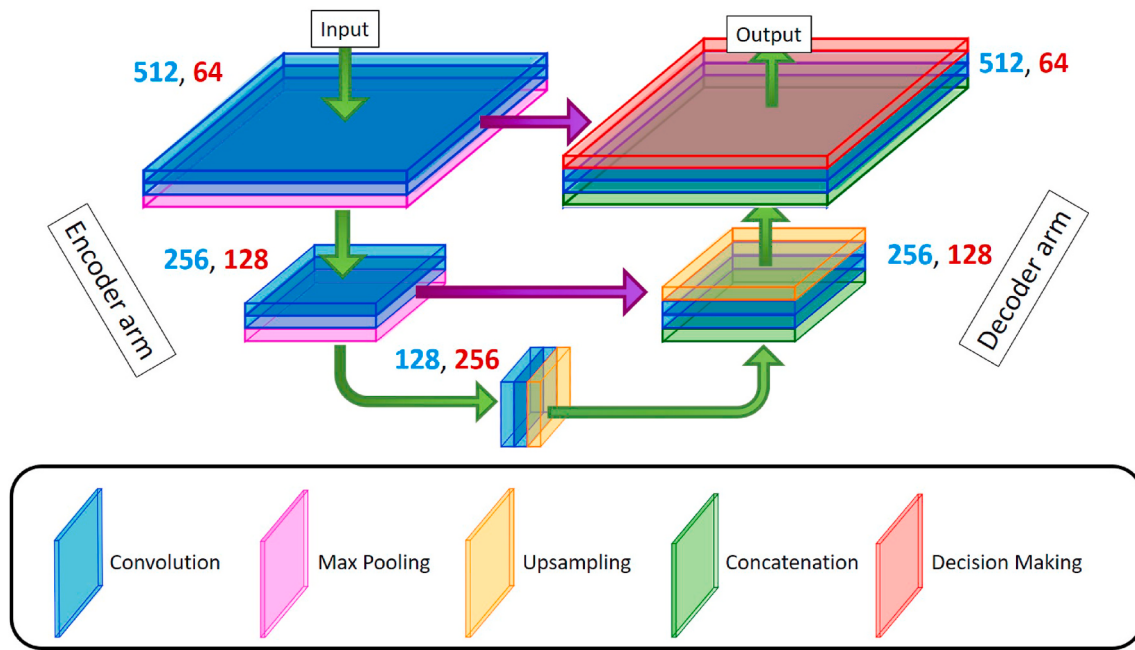


**Fig. 9.** Simple U-net-like convolutional neural network (CNN). U-nets form the basis of many state-of-the-art image segmentation algorithms. Following the green arrows in the network diagram above indicates where this network architecture got its name. U-nets are often employed in medical imaging to perform semantic segmentation. In the encoder arm, the input image is downsampled with max pooling layers in order to help learn features. In the decoder arm, the learned feature maps are upsampled to produce a segmented image the same size as the input. In U-nets skip connections (purple arrows) concatenate feature maps in the encoder arm's outputs to inputs in the decoder arm. These skip connections help the network to maintain resolution in the segmented output. Blue and red numbers next to the network layers indicate the size of the input data at each layer and the number of output feature channels, respectively.

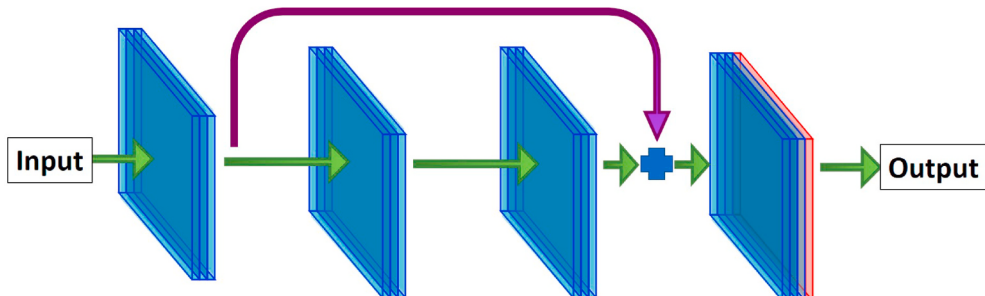


**Fig. 10.** Example resnet-like module. Resnets form the basis of many state-of-the-art image classification networks. In Resnets, skip connections (purple arrows) link the outputs of shallower convolution layers (blue layer) with deeper through addition. Multiple modules such as the one pictured can be chained together to create very deep networks, before the output is determined by a decision making layer (red layer).

angiograms directly from structural OCT scans. This transforms OCTA signal generation from a motion contrast measurement to an image translation problem. Image translation is a well-studied branch of machine learning, with applications in super-resolution image reconstruction (Dong et al., 2016; Kim et al., 2016), denoising (K. Zhang et al., 2017), and synthesis (Isola et al., 2017; Zhu et al., 2017).

Leveraging image translation expertise to construct angiograms via deep learning has some practical advantages. For one, signal generation in OCTA measures motion contrast, when what we are really interested in is flow signal. Learning-based approaches, on the other hand, could learn to distinguish flow and static voxels using any image statistics (rather than just motion contrast), which could provide a more accurate approach. This speculation receives some experimental support from Liu et al. (2019), who used a modified image denoising convolutional neural network (CNN) (Zhang et al., 2017) trained on sets of four registered B-frames (Lowe, 1999) from sets of 38 sequential data volumes captured from rodent models. Later, Jiang et al. found that U-net-like (Ronneberger et al., 2015) and multi-model path architectures (Xu et al., 2018) outperformed both single path (Zhang et al., 2017) and generative

adversarial networks (GANs) (Goodfellow et al., 2014) in this task (Jiang et al., 2020b). Both of these networks outperformed split-spectrum amplitude and phase-gradient angiography processing even when the number of input channels was reduced to two (the number used by the most efficient OCTA algorithms, including split-spectrum amplitude-decorrelation (SSADA) and optical microangiography (OMAG)). A similar GAN architecture (Ma et al., 2018) can extract angiograms from rodent images using 3 input B-scans (P. L. Li et al., 2020).

Learning differences between speckle patterns in blood flow and static tissues from multiple B-scans is ultimately similar to determining motion contrast through traditional means; the principle behind flow signal generation is still fluctuation in the OCT signal between consecutive measurements. Another approach is to extract angiograms from single structural OCT B-scans (Lee et al., 2019) (Fig. 11). The shorter OCTA scan acquisition times required with this approach mean that motion artifacts will be restricted. Furthermore, such algorithms could in principle recover angiographic information from currently available clinical OCT scans in which an OCTA scan pattern was not applied, potentially increasing the amount of data available for OCTA

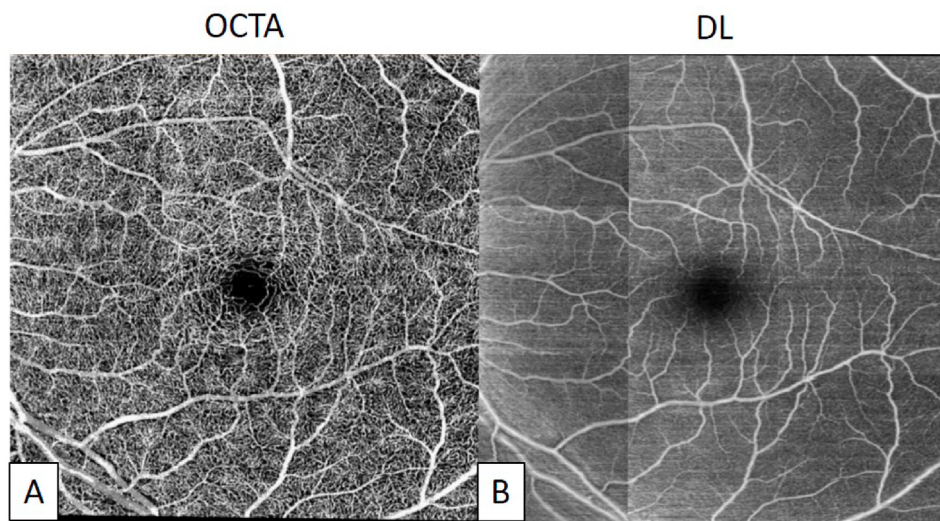


**Fig. 11.** OCTA signal generation from a single B-frame using deep learning. (A) A macular OCTA image from a Zeiss Angioplex instrument. (B) A flow map of the same eye generated by deep learning (DL). The ability to generate OCTA-like data from single B-frames would improve on image acquisition times. Reprinted with permission from (Lee et al., 2019).

quantification and development. However, extracting angiographic information from just a single B-scan is more challenging than extracting the same information from sequential scans. The method due to Lee et al. fails to capture some capillary details that can be obtained from OCTA (Lee et al., 2019).

Rather than generating OCTA data *ex novo*, convolutional neural networks can also be applied directly to OCTA data to improve image quality. One of the major limitations of contemporary OCTA is a limited field-of-view. Some OCTA scanning protocols increase the field-of-view by sacrificing A-line density. This leads to low definition scans that are more likely to contain artifacts and are generally of lower quality. Gao et al. trained a CNN to reconstruct capillary details that are vague and indefinite in low-definition, wide-field scans by using registered (Klein et al., 2010) high-definition scans as the ground truth and employing a structural similarity index for a loss function (Gao et al., 2020) (Fig. 12).

Perhaps surprisingly, the network used in this work was also capable of improving scan quality in high definition scans. Similar image quality improvement was traditionally secured through handcrafted filters (Frangi et al., 1998), but these appear to return less significant improvements in image quality as assessed by signal-to-noise ratio, image contrast, and vascular continuity.

We anticipate that OCTA reconstruction and enhancement on *en face* angiograms can be more efficient and practical than OCTA signal generation by deep learning using multiple B-frames. In particular, training paradigms that rely on upwards of 30 sequentially captured B-frames would be difficult to secure in a clinical setting. Image reconstruction networks offer the potential to improve OCTA image quality without inducing problematic data acquisition requirements.

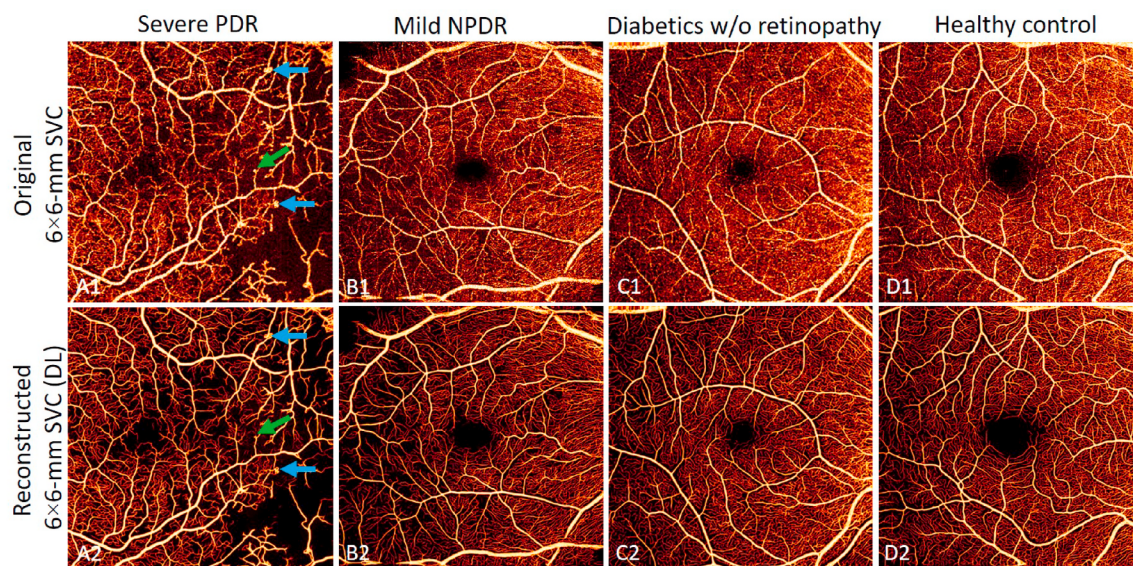
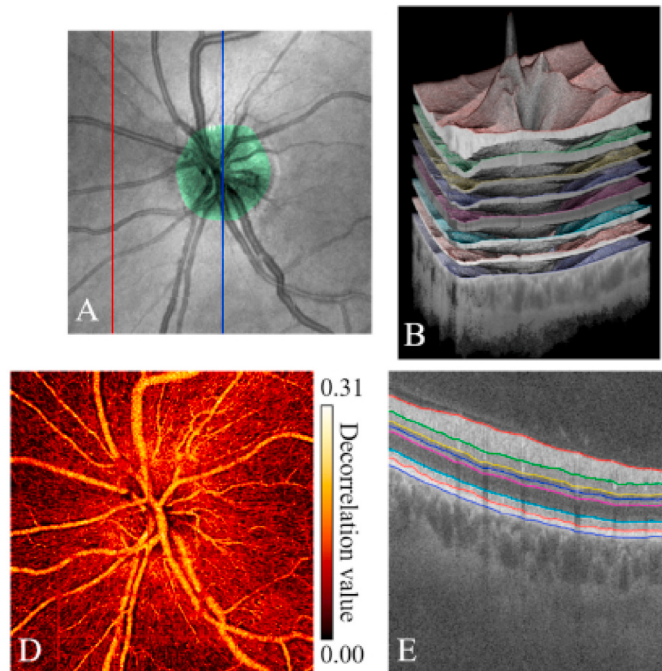


**Fig. 12.** *En face* OCTA image reconstruction using a convolutional neural network (CNN). (Top row): Original 6 × 6-mm OCTA *en face* images of a patient with severe proliferative diabetic retinopathy (PDR), mild non-proliferative diabetic retinopathy (NPDR), a diabetic without retinopathy, and a healthy volunteer. (Bottom row): Equivalent images after reconstruction using a CNN. The CNN used in this work was trained to reconstruct low definition 6 × 6-mm OCTA images by optimizing a structural similarity loss function which minimized the difference between the original 6 × 6-mm image and a registered high definition 3 × 3-mm *en face* image of the same eye. Arrows in column 1 indicate pathology (microaneurysms: blue; venous beading: green) that was preserved in the reconstructed angiogram.

#### 4.1.2. Retinal slab segmentation

Retinal slab segmentation is a final piece essential to generate *en face* OCT angiograms of each capillary plexus (see section 2.2). The first retinal slab segmentation algorithms worked by identifying features in the axial reflectance profile and correlating these with anatomic features (Ahlers et al., 2008; Baroni et al., 2007; Cabrera Fernández et al., 2005; Dai and Sun, 2011; Fabritius et al., 2009; Ishikawa et al., 2005; Shahidi et al., 2005; Tan et al., 2008). Most of these methods predated or were roughly concurrent with the first successful flow detection due to OCTA (Makita et al., 2006), and so were often employed as a processing step in order to extract retinal thickness measurements, which can be useful for diagnosis and monitoring in glaucoma (Hood and Kardon, 2007; X. Zhang et al., 2017) and edema (Diabetic Retinopathy Clinical Research Network, 2008). Axial reflectance profiles, however, are vulnerable to changes in magnitude due to speckle variation, pathology such as retinal fluid or drusen, and low image contrast. These variations can cause features in the reflectance profile to disappear. As a result, axial-reflectance-based methods are not especially robust. Semi-automated procedures can improve performance (Szkulmowski et al., 2007; M. Zhang et al., 2015), but at the cost introducing a potentially labor-intensive step into the analysis pipeline.

Many different edge detection and segmentation algorithms have been levied to produce satisfactory segmentation of retinal slabs (Kass et al., 1988; Mishra et al., 2009; Mujat et al., 2005). Most of these methods have been replaced by deep-learning-based approaches, but one method that has been historically widely employed and still retains usefulness today is graph search (Antony et al., 2010; Chiu et al., 2010; E. Gao et al., 2017; Garvin et al., 2008; Guo et al., 2018b; Haeker et al., 2007; Kafieh et al., 2013; Karri et al., 2016; Shi et al., 2015; Srinivasan et al., 2014; Yang et al., 2010; Zang et al., 2017a). This method phrases boundary determination as a network traversal problem, which can be efficiently solved using a directional (M. Zhang et al., 2015) or bidirectional search (Guo et al., 2018b) and dynamic programming (Zang et al., 2017a). One virtue of graph search is that it can complement other methods to refine the edges that they produce. In this context, graph search has found recent use in combination with machine-learning-based methods (Kugelman et al., 2018; Miri et al., 2015; Srinivasan et al., 2014; Zang et al., 2019) to refine the boundaries they produce (Fig. 13).



Like other image processing tasks in medical imaging, retinal slab segmentation benefits from machine learning. Support vector machines (Srinivasan et al., 2014; Vermeer et al., 2011), prior information models (Dufour et al., 2013), and structured forests (Karri et al., 2016) have all been explored in this context. Contemporary research has tended to replace machine learning techniques like these with deep learning, i.e. CNN architectures (Devalla et al., 2018; Fang et al., 2017; Pekala et al., 2018; Sui et al., 2017; Zang et al., 2020).

One of the reasons for the proliferation of slab segmentation techniques in the literature is the need for such algorithms to function in a variety of contexts. Specifically, some pathologies can introduce profound distortions to the retina (Das et al., 2018; Prager et al., 2014; Sun et al., 2015). This means that algorithms characterized on healthy retinas may not perform reliably on diseased eyes, and calls for specifically designed algorithms to respond correctly to pathologic changes like pigment epithelial detachments (Shi et al., 2015), retinal fluid (Bai et al., 2017; Chiu et al., 2015), or glaucoma-induced nerve fiber layer thinning (Antony et al., 2010). With deep learning, models can also be optimized for accuracy segmenting retinal slabs for eyes with a specific disease (Fang et al., 2017; Kugelman et al., 2018). Such approaches can have the advantage of identifying fluid regions as separate entities from the anatomic slabs that surround them. Even in the absence of pathology different anatomic regions may require separate retinal slab segmentation algorithms. For example, most algorithms are designed separately for the macula (Guo et al., 2018b), optic nerve head (Devalla et al., 2018; Zang et al., 2019), or choroid (Sui et al., 2017). Finally, children (Kugelman et al., 2018) and other species (Srinivasan et al., 2014) may both also require specifically designed solutions.

#### 4.2. Artifact removal or suppression

It is also possible to use AI to identify or remove specific artifacts.

##### 4.2.1. Bulk motion artifacts

Bulk motion artifacts due to microsaccades manifest as extremely disruptive bright stripes. As noted, they can often be removed through hardware approaches (Camino et al., 2016b; Wei et al., 2020b; Zang et al., 2016) or registration of different priority scan patterns (Camino et al., 2016a; Hendargo et al., 2013). However, in extreme cases residual

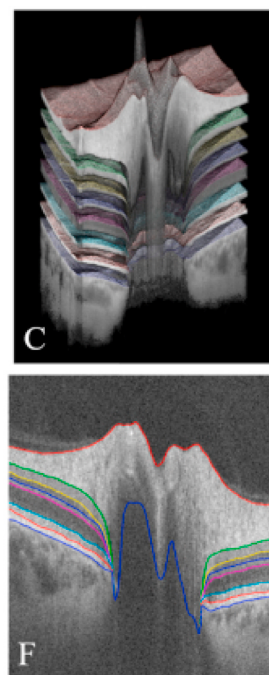


**Fig. 13.** Peripapillary retinal slab segmentation using a convolutional neural network. (A) *en face* average projection, with the segmented optic disc region overlaid in green. (B) Anatomic map of the entire volumetric OCT based on the segmented peripapillary retinal layers. (C) Cutaway from (B) at the blue line location in (A), clearly showing the anatomic structure inside the disc. (D) *en face* superficial vascular complex angiogram based on these segmented boundaries. (E) B-frame corresponding to the red line in (A) with segmented peripapillary retinal boundaries. (F) Corresponding image for the blue line in (A). The slab boundaries are, from top to bottom, the vitreous/inner limiting membrane (red), nerve fiber layer/ganglion cell layer (green), inner plexiform layer/inner nuclear layer (yellow), inner nuclear layer/outer plexiform layer (blue), outer plexiform layer/outer nuclear layer (magenta), outer nuclear layer/ellipsoid zone (cyan), ellipsoid zone/retinal pigment epithelium (red) and retinal pigment epithelium/Bruch's membrane (blue). Reprinted with permission from (Zang et al., 2019).

microsaccadic artifacts will remain, since in both cases information will still be missing from the scans lost to microsaccade or replaced with hardware rescan. Instead of replacing these missing frames, Hossbach et al. trained a U-net-like CNN architecture to generate angiographic data for the microsaccade-affected B-scans (Hossbach et al., 2020).

Bulk motion due to slower forms of motion, such as ocular pulsation and drift, can also be corrected with AI. Phase- and complex-signal-based OCTA protocols all incorporate bulk motion removal algorithms, but these often just estimate bulk motion based on a single test statistic (Makita et al., 2006; Mariampillai et al., 2010). A regression-based bulk motion removal technique that sequentially estimates the bulk motion contribution from OCT reflectance correlations more completely removes bulk motion, as gauged by image signal-to-noise ratio and contrast (Camino et al., 2017) (Fig. 14). This algorithm has been shown to improve image quality in multiple devices (Camino et al., 2018b).

#### 4.2.2. Shadowing artifacts

Shadowing artifacts are especially problematic since in severe cases signal attenuation can completely eliminate the reflectance signal. In such cases the best we can do is detect artifact-affected regions in order to exclude them from quantification. Failing to exclude shadow artifacts from analysis inaccurately reduces vessel density and could lead to erroneous detection of non-perfusion areas (NPA).

While they cannot be removed, shadow artifacts can still be identified based on their signal in both the structural OCT and OCTA data sets. Shadowing artifacts indiscriminately darken both structural OCT and OCTA signals, and this simultaneous occurrence can be used by intelligent algorithms. Random forests are a deep learning technique built around decision trees. With sufficient depth, they have been shown to be capable of accurately segmenting shadow-affected regions (Camino et al., 2019) (Fig. 15). And, like any feature that can be segmented manually, with sufficient data a CNN can learn to detect shadows. Because shadowing artifacts can so easily be conflated with NPA, state of the art non-perfusion area segmentation should also include shadow detection. In one approach, Guo et al. incorporated a CNN with a U-net-like architecture trained to detect shadows into their NPA segmentation algorithm (Guo et al., 2019). The full algorithm is an example of deep-learning-aided OCTA feature quantification, which we will now discuss.

#### 4.3. OCTA feature analysis

Features detectable by OCTA may be resistant to simple or swift manual quantification. Examples include NPA, just alluded to, which requires calculation of the distances to vessels—an arduous procedure even when semi-automated. Other biomarkers, such as choroidal neovascularization (CNV), would be easier to quantify were it not for the fact that they occur in an artifact-rich environments. Furthermore, even when quantification may be straightforward, AI can often offer performance superior to more elementary algorithms.

##### 4.3.1. Vessel density and segmentation

Vessel density is frequently measured in OCTA. In part this can be attributed to the ease with which it can be measured, since vessel density values can be extracted through thresholding (Chidambara et al., 2016; Eladawi et al., 2017; Hwang et al., 2016). But vessel density is also often measured because it is a valuable metric. It correlates with disease severity in several prevalent eye diseases including diabetic retinopathy (DR) and glaucoma (Jenkins et al., 2015; Jia et al., 2014b; Nesper et al., 2017). Nonetheless, some limitations in vessel density should be noted. First, vessel density measurements correlate with OCTA signal strength (Yu et al., 2019). This means that without calibration vessel density measurements will be less discriminatory for diagnostic purposes than they could be. Second, while vessel density measurements made using the same method with data from the same instrument are highly repeatable (Al-sheikh et al., 2017; Lei et al., 2017b), measurements made using different methods or instruments are not necessarily interchangeable (Rabiolo et al., 2018).

Extracting vessel density measurements from an OCTA images is ultimately a segmentation task, and therefore amenable to solution using deep learning approaches like U-nets. A CNN model has been applied to segment vessels in the choroid (Liu et al., 2019), a more difficult task than in the retina due to the high density of larger caliber vessels in the choroid and stronger signal attenuation in deeper tissue. This work produced vessel density measurements that were consistent than those produced by manual segmentation. CNN-assisted vessel segmentation has also been shown to perform comparably to manual segmentation (Prentasic et al., 2016). A different U-net-like model can erase differences in vessel density measurements between instruments, and more robustly contend with the presence of disruptions due to projection artifacts (Heisler et al., 2019) (Fig. 16). Finally, vessel segmentation could also be improved by image enhancement techniques, since with improved image quality the difference between flow and

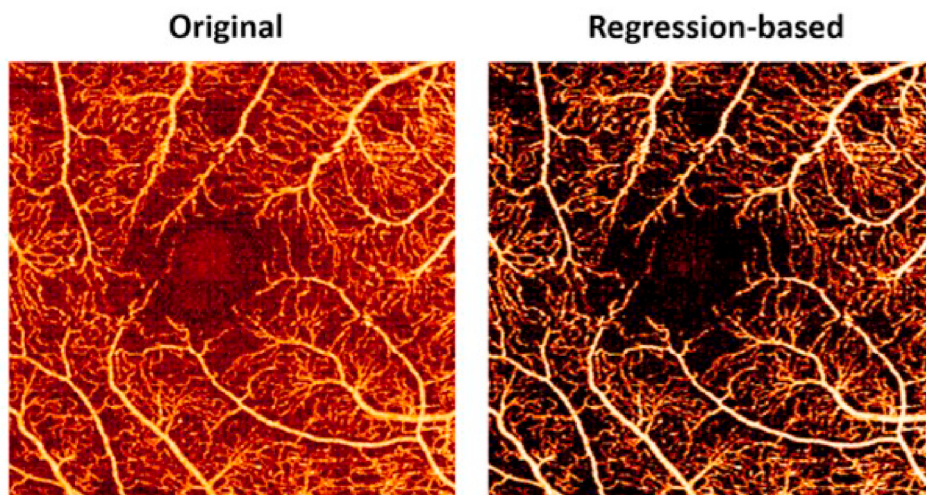


**Fig. 14.** Regression-based bulk motion subtraction. In the original image, the large background is due to the presence of bulk motion. In the regression-based corrected image, the bulk motion has been removed, leading to a larger contrast between the vasculature and surrounding tissue.

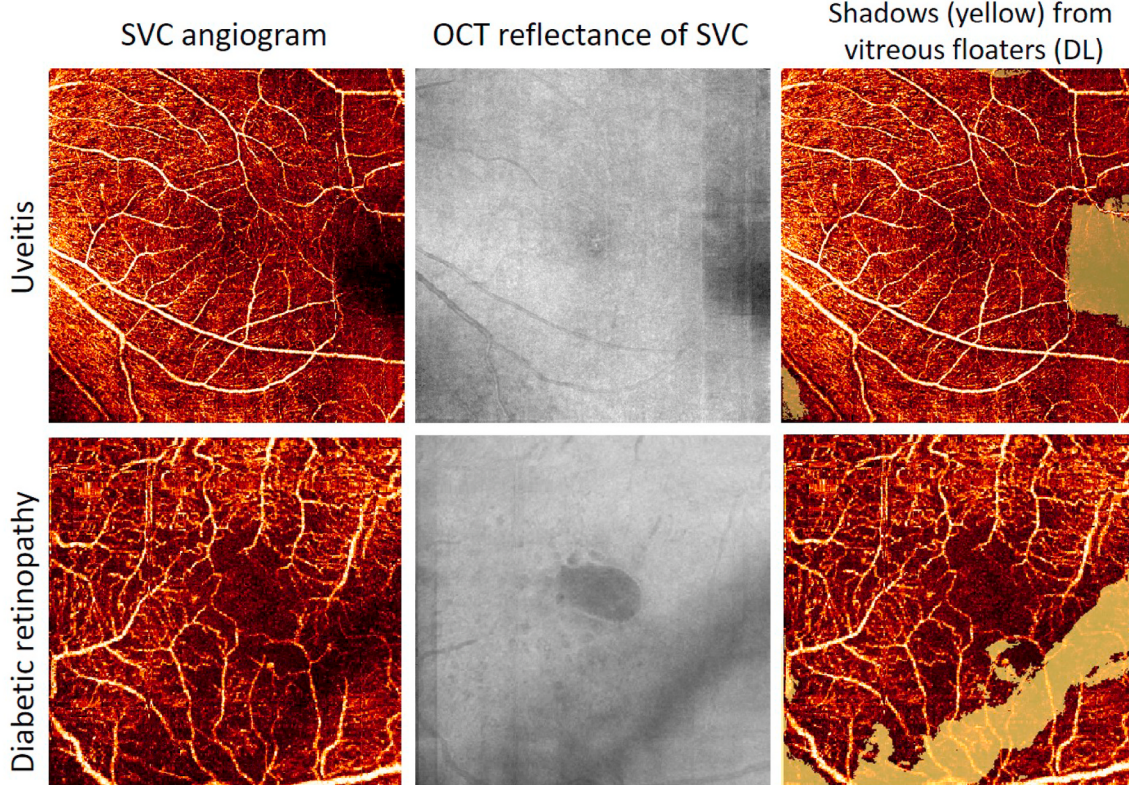


**Fig. 15.** Shadowing artifact detection using deep learning. Shown are an eye with uveitis (top row) and diabetic retinopathy (bottom row). The approach used in this work detected shadowing artifacts using a random forest model taking *en face* OCTA and OCT reflectance images of the superficial vascular complex (SVC) as input (Camino et al., 2019). The combination of both the structural OCT and OCTA data is a powerful means for intelligent algorithms to identify shadows, since they can learn that shadows coincide in both channels.

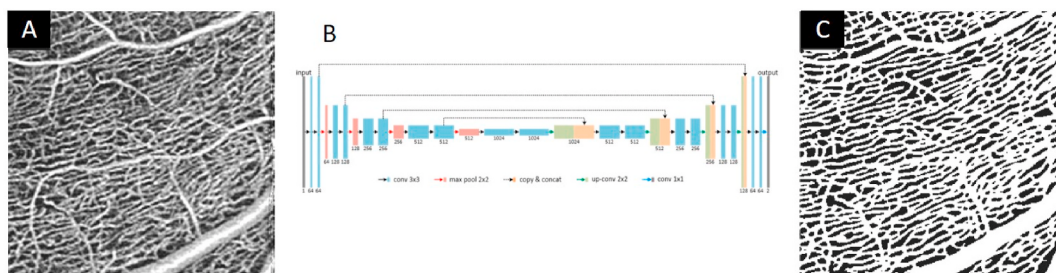


**Fig. 16.** Vessel segmentation using a deep learning. Here, the input (A) consists of a quadrant cropped from a  $6 \times 6$ -mm OCTA *en face* image. (B) The network architecture used in this study was U-net-like, with skip connections between an encoder and decoder arm. (C) The network outputs a binary vessel map. The segmentation produced by this network improved perfusion quantification in diabetic retinopathy. Adapted with permission from (Heisler et al., 2019).

background pixels is more apparent (Gao et al., 2020). Like most OCTA measurements, these methods operate on *en face* images, which is a tacit requirement for accurate anatomic slab segmentation. An alternative is provided by an image projection network, which uses CNNs to simultaneously extract features and perform projection (Li et al., 2020). This network achieved a higher Dice coefficient (which measures the overlap between the network result and the ground truth) than alternative architectures that followed the usual analytic pipeline in which OCTA data sets are projected within a specific plexus before quantification.

#### 4.3.2. Differentiating arteries and veins

Diseases can affect arteries and veins asymmetrically and differential artery-vein analysis in OCTA data has been shown to improve staging in sickle cell retinopathy (Chen et al., 2018; Klein et al., 2012). These studies indicate that differential artery-vein analysis in OCTA has clinical potential, but OCTA data is insensitive to flow direction. It is

impossible to determine whether a vessel is a vein or artery just by considering the flow magnitude. Instead, artery/vein classification in OCTA has to be informed by anatomic and morphological considerations (Alam et al., 2020b), or supplemented with complementary information from other modalities (including structural OCT) (Alam et al., 2018, 2019b; Son et al., 2019).

Alam et al. have tested a U-net-like CNN that was able to identify arteries and veins with  $86.751 \pm 1.126$  percent accuracy (Alam et al., 2020a). In order to generate a ground truth for this network, they registered the *en face* OCTA images with color fundus photos; the network also included structural OCT information as input since some structural features can be useful for artery-vein determination (Alam et al., 2019b). Enhancing images with a deep learning network as a processing step in an artery/vein identification analysis pipeline is a good example of the use of AI image reconstruction to improve quantification, since noise reduction can improve the accuracy of

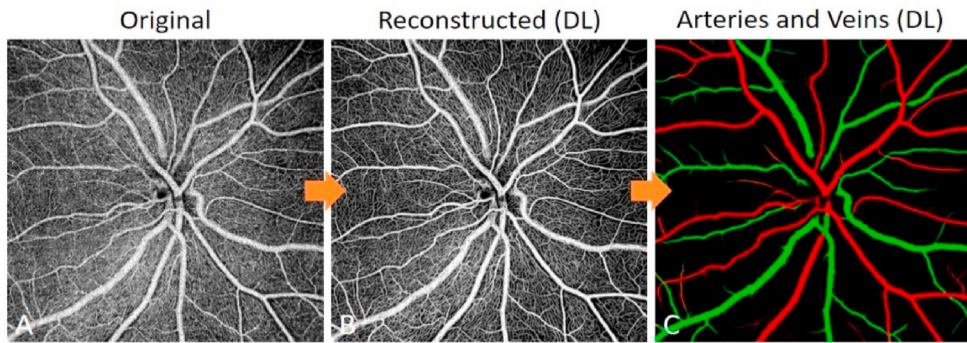


**Fig. 17.** Artery and vein classification using deep learning. (A) A raw  $4.5 \times 4.5$ -mm,  $400 \times 400$ -pixel OCTA *en face* image of the optic nerve head. This image serves as the input to an image reconstruction deep learning (DL) network. (C) The DL reconstructed image is used as the input to another DL network, this one trained to identify arteries and veins from a manually delineated ground truth.

morphological measurements (Fig. 17).

#### 4.3.3. Non-perfusion area

Vessel density measurements usually quantify perfusion loss across an entire image. However, perfusion loss in some diseases- DR, for example-is frequently confined to specific regions (Niki et al., 1984). This pattern of perfusion loss is better captured by calculating non-perfusion area (NPA), which is consequently more sensitive to DR progression than vessel density (Schottenhamml et al., 2016). A NPA is defined as any pathologically avascular patch above a size threshold, and can be measured automatically by calculating distance maps after vessel segmentation (Schottenhamml et al., 2016; Zhang et al., 2016b). However, more robust results can be achieved with a deep learning (Guo et al., 2018a).

NPA detection combines several problems that require powerful

software solutions. Foremost is the resemblance of NPA to shadowing artifacts. Though they are superficially similar, intelligent combinations of structural OCT and OCTA data can distinguish NPA and shadowing artifacts (Guo et al., 2019) (Fig. 18). The algorithm due to Guo et al. achieved at least 95% accuracy for NPA detection in every stage (mild or moderate DR, severe DR, diabetes without DR, and healthy controls) of DR examined, and was also resistant to image quality effects (Fig. 19).

Like other quantification in deeper layers, NPA detection in the ICP and DCP is a significantly more formidable problem than in more superficial layers. This is due to the presence of projection artifacts and the generally lower signal quality found in deeper layers. A different CNN network design incorporating U-net-like architectures has shown strong performance in this task (Wang et al., 2020b) (Fig. 20). The authors noted that the algorithm's performance was strongest for healthy individuals in the SVC, and worst amongst severe DR patients in the DVC

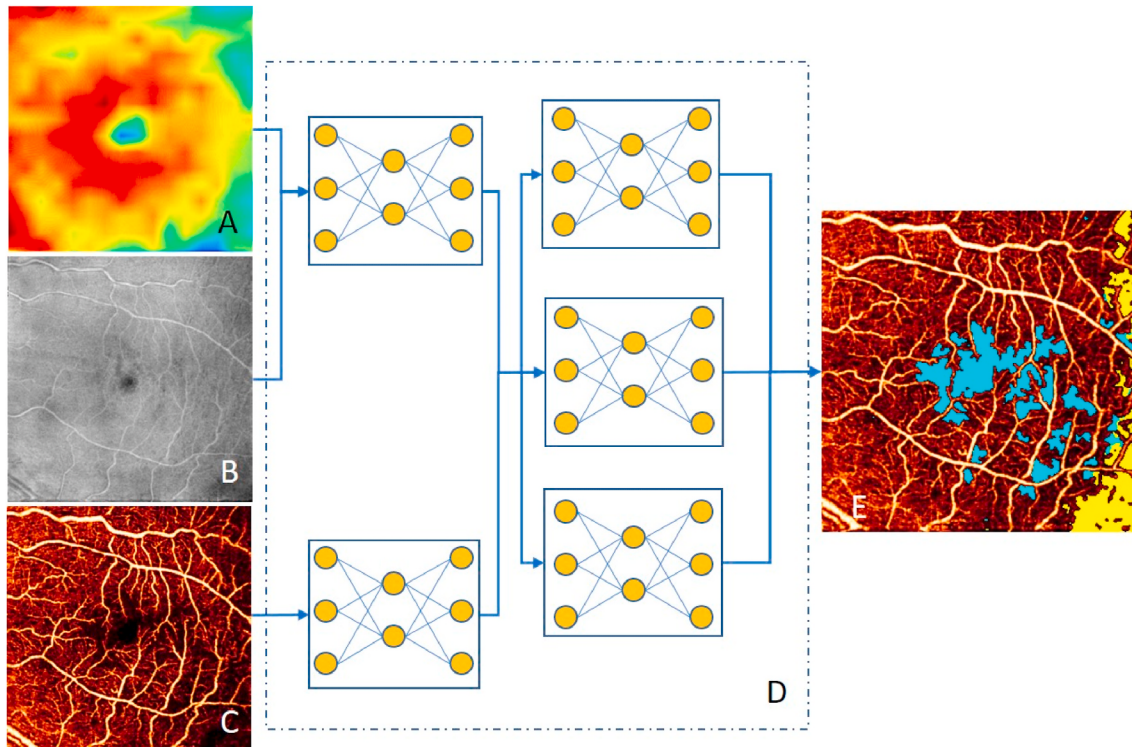


**Fig. 18.** Network architecture (Guo et al., 2019) for a non-perfusion area (NPA) segmentation algorithm. Inputs to the model include a retinal thickness map (A), as well as structural OCT (B) and OCTA (C) *en face* images of the superficial vascular complex. (A) and (B) are fed into a convolutional neural network (CNN) that learns to extract features relevant for shadow detection, while (C) is fed to a separate network that learns features associated with NPA. The output from each of these networks is then used as input to a series of three parallel CNNs that vote to determine whether a region is NPA (blue), shadow (yellow), or vascular.

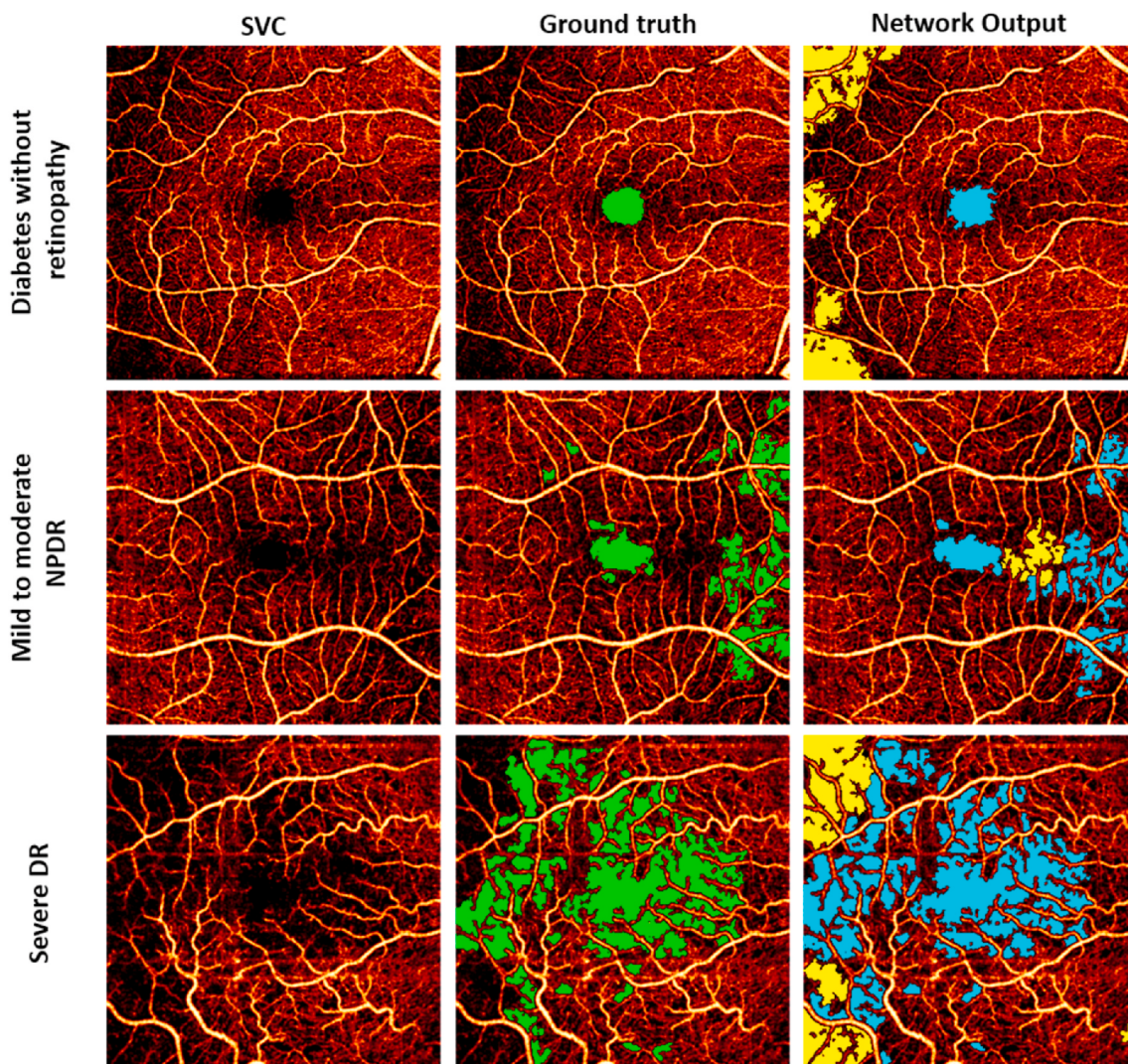


**Fig. 19.** Non-perfusion area (NPA) detection using a convolutional neural network (CNN) (Guo et al., 2019). Shown are an eye with diabetes but not retinopathy, and eye with moderate non-proliferative diabetic retinopathy, and an eye with severe diabetic retinopathy. Column 1 shows unmodified superficial vascular complex (SVC) angiograms, while column 2 shows an expert generated ground truth (green), and column 3 shows the network output. The CNN is capable of distinguishing NPA (blue) from shadowing artifacts (yellow), despite their similar appearance.

(F1 score =  $0.97 \pm 0.03$  and  $0.78 \pm 0.07$ , respectively). This is unsurprising, however the fact that the network's performance on the harder task (detection in low-signal regions of pathological eyes) does not achieve parity indicates either better artifact removal or more training data are required for CNNs to meet their potential here.

#### 4.3.4. Choroidal neovascularization

Another important biomarker in OCTA imaging is neovascularization. Retinal neovascularization (RNV) and choroidal neovascularization (CNV) are important developments in two of the leading causes of blindness, DR and age-related macular degeneration (AMD), respectively (Antonetti et al., 2012; Flaxman et al., 2017; Mitchell et al., 2018). Due to its anterior location, RNV is typically easier to quantify than CNV. In particular, with accurate retinal slab segmentation RNV can be identified based on its location above the inner limiting membrane (Gao et al., 2017; Liu et al., 2015).

Due to the presence of projection artifacts and signal attenuation, accurate quantification and identification of CNV is much more difficult. In particular, projection artifacts appear very similar to CNV since they retain the vascular characteristics of the vessels that generated them. Furthermore, projection artifacts can appear on top of real CNV, detrimentally influencing any related quantifications. Even with successful

projection artifact removal, CNV can take on a number of morphologies and characteristics, which require contextual information in order to identify. These complications mean that even intelligently crafted image analysis procedures such as saliency mapping will not perform well on some scans (Liu et al., 2015).

Deep learning networks can perform robustly despite these same complications (Wang et al., 2020a). However, since this is a difficult problem lacking large stores of data to train a deep learning network with, intelligent architectural and input choices are required. The network design due to Wang et al. uses a large catalog of inputs (Fig. 21). The input list ensured that the network had access to the contextual information that it required to correctly quantify CNV (Fig. 22). Wang et al. also trained two specialized networks for this task: a diagnostic network that diagnoses CNV based on the CNV lesion size, and vessel segmentation network specialized to segment vessels from the input membrane image. The algorithm achieved a diagnostic accuracy of 95%.

#### 4.3.5. Retinal fluid

Even features that are not traditionally associated with vasculature can be improved by the inclusion of OCTA data. Because of its centrality to much of the diagnostic potential of structural OCT, the literature contains numerous retinal fluid segmentation methods (Bai et al., 2017;

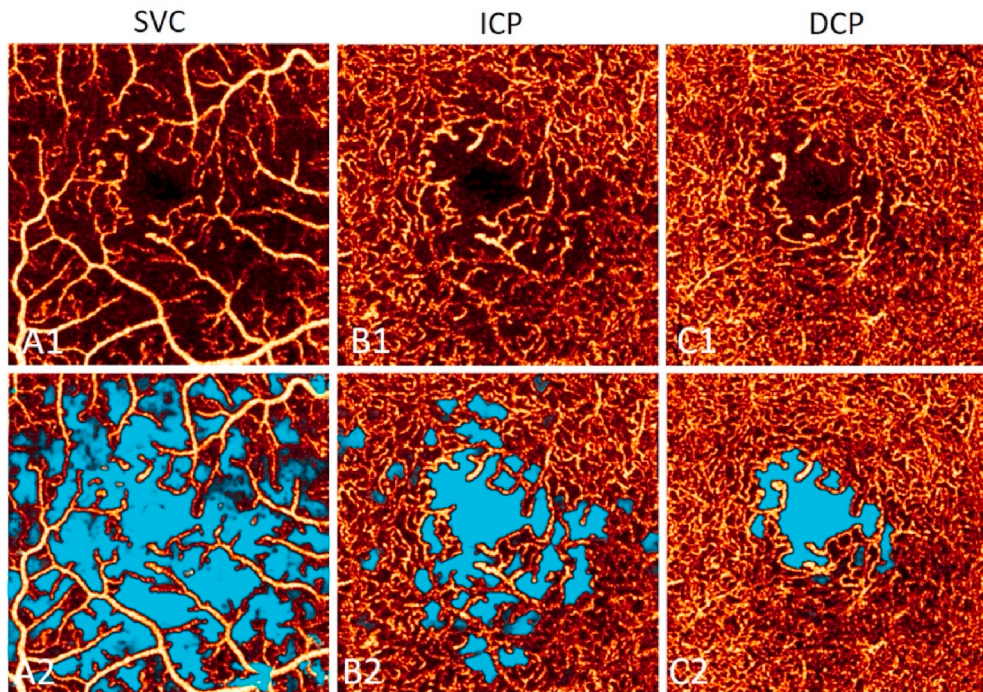


**Fig. 20.** Non-perfusion area detection using deep learning (Wang et al., 2020b). (Top row) *En face* OCTA images of an eye with severe non-proliferative diabetic retinopathy shows large non-perfusion areas in the deep (DCP) and intermediate (ICP) capillary plexuses, and especially in the superficial vascular complex (SVC). (Bottom row): A neural network outputs the probability that a pixel is part of a non-perfusion area (teal).

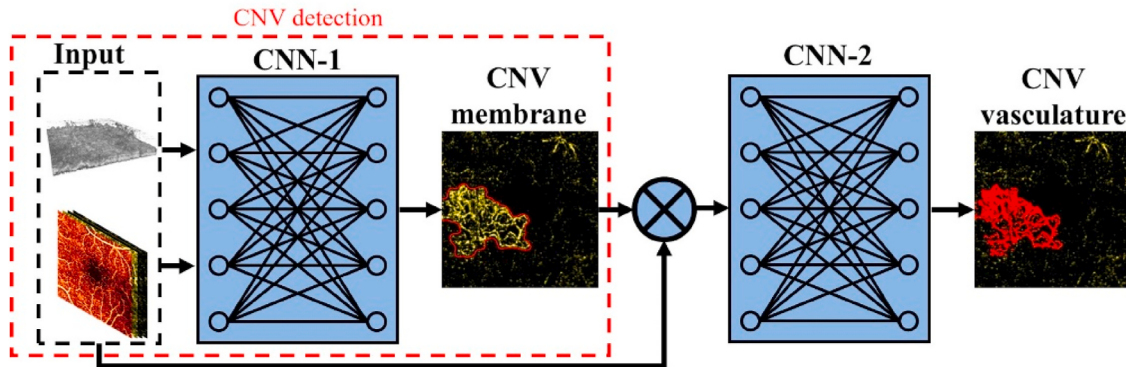


**Fig. 21.** Choroidal neovascularization detection and segmentation network architecture. In order to help distinguish CNV from projection artifacts, the network takes a raw inner retinal angiogram and raw, slab-subtracted, and projection-resolved (PR) outer retinal angiograms, and volumetric structural data from the outer retina as input. A CNN trained to segment the CNV lesion area diagnoses CNV based on the measured lesion size. If a lesion is detected, a second CNN will segment the CNV vessels. Reprinted with permission from (Wang et al., 2020a).

Gopinath and Sivaswamy, 2019; Lee et al., 2017; Lu et al., 2017; Montuoro et al., 2017; Thakur et al., 2018). While retinal fluid is more readily identified in structural OCT than from OCTA, retinal fluid does still have a signature in the OCTA channel since vessels do not occur in fluid regions. The OCTA channel, then, contains some complementary information for fluid segmentation. Guo et al. have quantified this contribution, finding that the same U-net-like architecture achieves the best performance when the input images were weighted to 20/80 OCTA/structural OCT (Guo et al., 2020). The same work is a justification for volumetric representations, since it clarified pathological cases where retinal fluid volume and projected 2D area could differ drastically. *En face* renderings can also make use of OCTA data in order to clearly identify the interplay between retinal fluid and vasculature (Fig. 23).

#### 4.3.6. Other features

There are many other vascular measurements and biomarker quantifications that can be collected from OCTA data. Foveal avascular zone (FAZ) area, for instance, can be quantified (Minvielle et al., 2016); however, FAZ area measurements are not particularly sensitive as a disease indicator due to the large variation in FAZ size in healthy eyes. For this reason, shape characteristics (Lu et al., 2018) or comparison to baseline statistics (Wang et al., 2019) are sometimes used to improve diagnostic performance. Any such metrics will be improved by more accurate FAZ segmentation, which can be achieved with a CNN (Heisler et al., 2019; Li et al., 2020). Dilated capillaries are another feature that can be detected automatically (Dongye et al., 2017). Photoreceptor loss, though not a purely vascular biomarker, can also be detected using OCTA data in combination with AI (Camino et al., 2018a; Wang et al., 2017). And a random forest algorithm has been used to characterize the

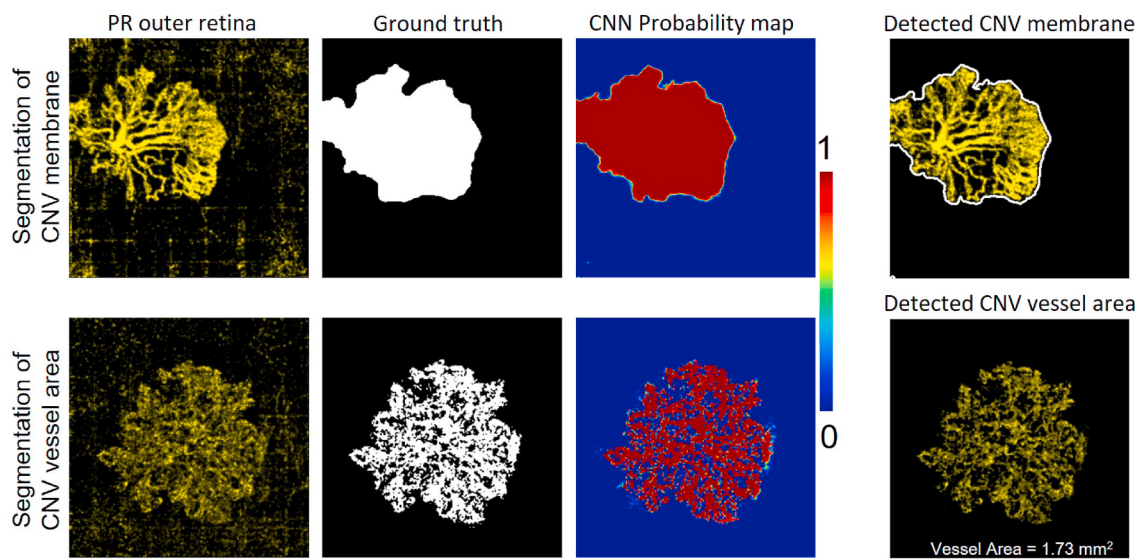


**Fig. 22.** CNV detection and vessel segmentation using deep learning according to Wang et al. (Wang et al., 2020a). Shown are two example images of CNV. In the top row, the CNV detection network was trained on a ground truth consisting of a segmented membrane area. It outputs an area similar to the ground truth with high probability. The network output consists of a segmented lesion area and a diagnosis of CNV if the detected membrane area exceeds a threshold value. The vessel segmentation network uses the membrane segmentation as input, and was trained on manually traced CNV vessels. It also outputs shapes similar to the ground truth with high probability. The vessel segmentation can be used to determine quantities such as the total vessel area. The network achieved an F1 score of  $0.93 \pm 0.08$  for lesion overlap area with the ground truth manual segmentation.

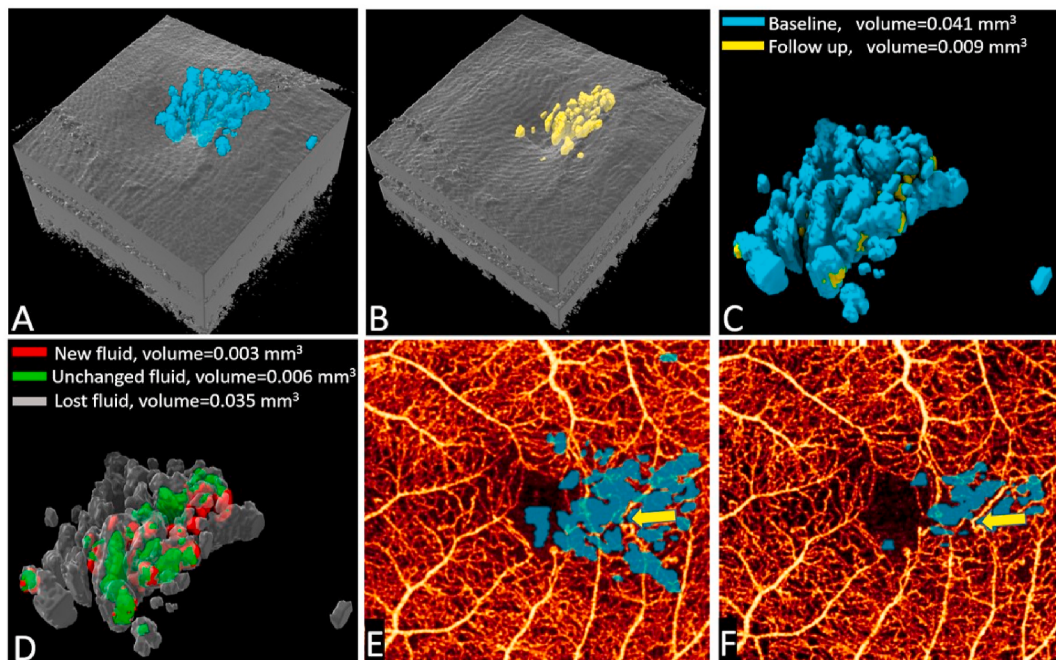


**Fig. 23.** AI-aided retinal fluid detection using structural OCT and OCTA data (Guo et al., 2020). This model segments retinal fluid from densely sampled volumes. (A-B) Automatically segmented retinal fluid at baseline (A; teal) and after treatment followup (B; yellow). (C) Overlaid fluid volumes. (D) The difference in volume at follow up shows that fluid volume has decreased. (E-F) En face OCTA images with fluid area overlaid. The combination of features shows vascular remodeling to avoid fluid volumes (yellow arrow).

choriocapillaris in choroideremia (Gao et al., 2017).

#### 4.4. Classification and diagnosis

##### 4.4.1. Intelligent combination of multiple features

Combinations of biomarkers and other features can be used in computer aided diagnostic (CAD) systems to help diagnose disease. Traditional approaches to this problem include techniques such as

logistic regression, but learned models can also perform such diagnosis. CAD systems that utilize OCTA data have been developed to diagnose DR at different severity levels (Sandhu et al., 2020). To do so, Sandhu et al. used a random forest model with structural OCT reflectivity, curvature, and thickness, and OCTA vessel caliber and density, the number of vessel bifurcations and crossover points, and FAZ size as input. This system achieved area under receiver operating characteristic curve values greater than 95% for distinguishing DR from non-DR eyes, and

grading severity in eyes already identified as having non-proliferative DR. A deep learning system that combines macular vessel density and ganglion cell/inner plexiform layer thickness has also been explored (Park et al., 2018). The AI-learned combination of these measurements outperformed either in isolation.

Deep learning has also been used in AMD diagnosis. Russakoff et al. found that a CNN can accurately predict eyes that will progress to advanced AMD from the intermediate form of the disease (Russakoff et al., 2019). And, as noted, since a CNN can be used to detect CNV (Wang et al., 2020a), deep learning can be used to classify the neovascular form of AMD.

CAD systems such as these will only be as strong as the feature measurements used as input. The continued improvement of feature quantification stands to benefit CAD systems. However, ultimately CAD systems are beholden to features that have been previously identified. This means that they cannot utilize information unrelated to the features incorporated in the design, even though this excluded information could be useful for diagnostic purposes.

#### 4.4.2. Feature agnostic OCTA diagnosis

A different approach to diagnostics foregoes feature quantification and attempts to detect pathology and disease directly from OCTA data. In part because it is easier to construct large data sets for prevalent diseases, this work has focused primarily on one such prevalent disease, DR. However, even DR datasets are still relatively small to train networks for this type of classification. As such, researchers have tended to resort to approaches that boost performance in limited data contexts. One example is transfer learning, in which parameter values learned for a different task are used to initialize training parameters. Using this approach, Le et al. achieved accurate (87.27%) identification of healthy eyes, diabetic eyes without retinopathy, and DR (Le et al., 2019). Another approach is ensemble learning, where several networks are trained individually to perform a single classification task. Ensemble learning algorithms then consider the output from each network in order to make a final composite prediction. Heisler et al. used this approach by

training separate networks to predict referable DR from superficial and deep structural OCT and OCTA data. They achieved a diagnostic accuracy of 90 or 92%, depending on how the ensemble prediction was performed (Heisler et al., 2020a). Another approach that can help networks achieve reasonable generalization from small data sets is adaptive label smoothing, in which class labels are adjusted during training to discourage overfitting. Zang et al. applied this approach to multiple levels of DR classification. They achieved a 95% classification accuracy for referable vs. non-referable DR identification, but a significantly lower accuracy (71%) for differentiating no DR, mild or moderate non-proliferative DR, severe non-proliferative DR, and proliferative DR (Zang et al., 2020). This last task is much more difficult than a referable vs. non-referable classification due to the similarities between some classes (e.g., moderate and severe non-proliferative DR eyes can be difficult to distinguish). Larger numbers of classifications also mean that fewer classes are available with each label during training.

One advantage of using CNNs to diagnose diseases directly from OCTA data is that such networks can produce class activation maps (CAMs), which can be used to visualize features that the network considered important for decision making (Fig. 24). Active regions will often contain biomarkers, so CAMs can serve as an effective means for clinicians to verify AI predictions. CAMs may eventually shed light on new features that can be used for disease diagnosis, and so could also be used as biomarker discovery tools.

One important hurdle that currently remains for OCTA diagnosis of retinal diseases is a lack of OCTA-specific diagnostic criteria. Gold standard DR diagnosis is determined by fundus photography, which does not have access to the same microvascular information as OCTA. This means that some staging determined by OCTA networks could be making reasonable predictions that are simply unverifiable with fundus photography. Alternatively, some features from fundus photography may not be available in OCTA. The best way forward to alleviate these concerns will be continued research into new OCTA biomarkers. With a comprehensive list of such biomarkers, new diagnostic criteria based on OCTA could replace reliance on fundus photography characteristics.

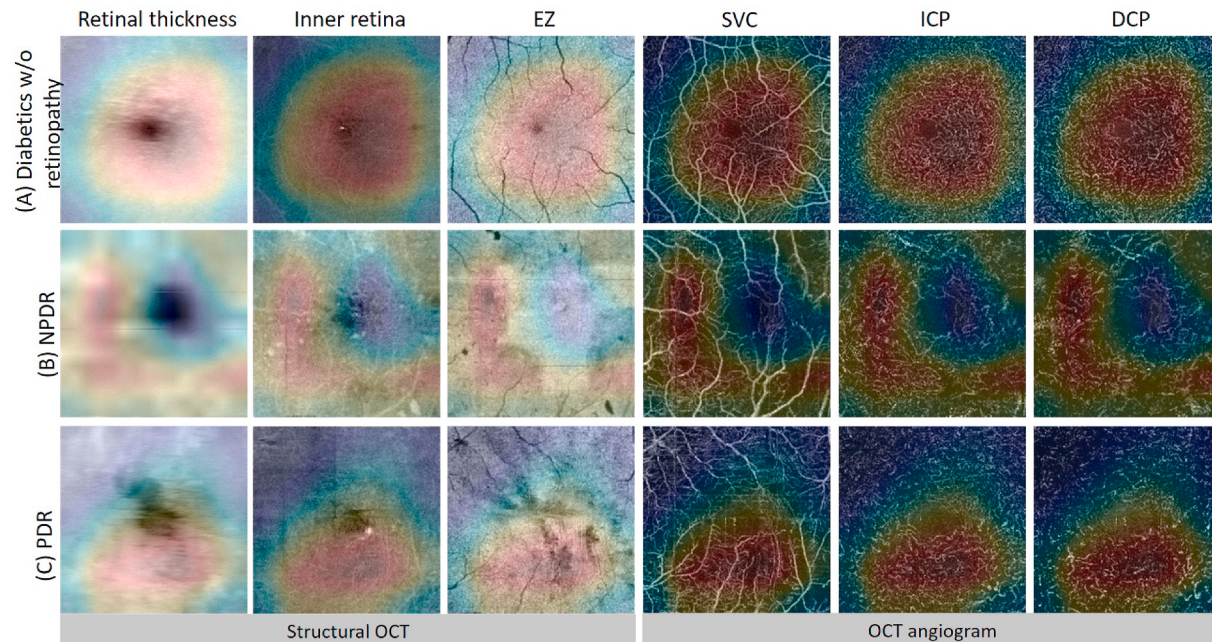


**Fig. 24.** Class activation maps (CAMs) for diabetic retinopathy (DR) classification. Shown are eyes correctly predicted by a convolutional neural network (CNN) as being diabetic without retinopathy (top row), having non-proliferative DR (middle row), and having proliferative DR (bottom row). This network, DcardNet, takes three structural OCT images (the retinal thickness map, and *en face* images of the ellipsoid zone and retina) and three OCTA images (the superficial vascular complex and intermediate and deep capillary plexuses) as input. The CAMs overlaid atop these inputs show which regions of the image the network considered important (red) or not (blue) for decision making; regions which the network paid attention to can coincide with known features. Reprinted with permission from (Zang et al., 2020).

**Table 2**

State of the art AI algorithms in OCTA by method and topic.

Task	Method	Publication
OCTA signal generation	CNN	Jiang et al. (2020a); Lee et al. (2019); Liu et al. (2019)
OCTA image enhancement	CNN	Gao et al. (2020)
Artifact removal	Random forest	Camino et al. (2019)
Feature segmentation	Regression CNN	Camino et al. (2017) Alam et al. (2020b); Alam et al. (2019a); Guo et al. (2020); Heisler et al. (2019); Liu et al. (2019); Prentašić et al. (2016); Wang et al. (2020b)
	Random forest	Gao et al. (2017)
Diagnosis	CNN	Alam et al. (2019); Heisler et al. (2020b); Le et al. (2019); Zang et al. (2020)

#### 4.5. Summary

**Table 2** summarizes state of the art AI techniques discussed in this section by topic and method.

#### 5. Future directions

OCTA has the potential to improve the standard of care for several retinal vascular diseases. Simply by virtue of working non-invasively, replacing dye-based angiography with OCTA when applicable will improve screening and monitoring. But OCTA can do more than simply recapitulate results from dye-based angiography. Studies have already shown that three-dimensional quantification of pathology-for example neovascular lesion complexity (Nesper et al., 2018) or 3D parafoveal vessel density (Wang et al., 2019)- can improve diagnostic and prognostic capability. Similarly, depth resolution in OCTA enables quantification of pathology within individual retinal plexuses, which also appears to offer advantages for clinical imaging and may enhance our understanding of disease pathophysiology (Hormel et al., 2020). However, the complexity of the information captured during an OCTA procedure and the size of the data sets themselves mean that manual analysis can be infeasible.

By enabling researchers and clinicians access to rich information latent in OCTA data, artificial intelligence can help OCTA imaging achieve its potential. With AI, tasks such as non-perfusion area segmentation, which would be enormously time-consuming to accomplish manually in large data sets, can be readily accomplished. In other cases, such as differentiation of veins and arteries, AI can extract features from images that are essentially impossible to characterize accurately by inspection. And some tasks, such as generation of OCTA signal from a single cross-sectional scan, we don't know how to approach without AI.

The best learning algorithm designs possible will still not provide adequate solutions to OCTA image analysis problems without access to data commensurate with their ambition. Data quantity and quality represents the largest hurdles for AI development. The literature already includes proof-of-concept algorithms for difficult, complicated tasks like diagnosis of disease directly from OCTA data volumes (Alam et al., 2019; Heisler et al., 2020a; Zang et al., 2020). However, we must await validation of many OCTA techniques in clinical trials. Again, due to the complexity of OCTA data analysis, these trials will almost certainly rely on some form of AI analysis.

Federated learning approaches, in which learning algorithms are trained from data spread across different locations and institutions, will be helpful to further validate AI-aided OCTA analysis. Federated learning can allow hospitals and universities to collaboratively train algorithms by combining data sets. Some collaborative OCTA data sets, such as ROSE (Ma et al., 2020), are publicly available; a comprehensive list of OCTA and other ophthalmological public data sets can be found in Khan et al. (2020). More than just an issue of quantity, federated learning can help with data quality by boosting representation of populations that may be under-represented in some data sets. International

collaborations especially can help fill out data sets with cases that rarely occur in a particular locality-for example, researchers in the United States can benefit from collaborations with East Asian institutions to procure polypoidal choroidal vasculopathy data, since that disease is relatively rare in the United States (Maruko and Iida, 2016).

These ideas all point toward the continued and growing relevance of AI in OCTA data analysis. With this in mind, we also believe that our current experience designing AI algorithms can inform design decisions going forward. We can identify the following design principles as important themes:

- (1) **A working knowledge of OCTA data acquisition and processing can inform algorithm design.** In particular, understanding the subtleties of OCTA technology can allow researchers to design to its strengths while avoiding its weaknesses. For example, researchers designing algorithms targeting quantification in deeper retinal anatomic layers should be aware of the detrimental effects of projection artifacts and incorporate some form of compensation in their methods. Researchers targeting perfusion metrics should be aware of the way that shadowing artifacts can complicate analysis. And researchers should be aware of the degrading influence of the low-density scanning patterns that are frequently used to expand the OCTA field of view. This list could go on. The point is that a working knowledge of OCTA technology can greatly boost performance by informing design choices.
- (2) **On the topic of design decisions:** one of the biggest choices in algorithm development is input selection. It is rarely if ever most straightforward to include the entire OCTA data volume as input. Rather, **intelligent selection of OCTA representations and data volumes can make image analysis tasks tractable** when they would otherwise be hopeless. Here again a firm understanding of OCTA technology can be useful. For example, if an algorithm will need to contend with shadowing artifacts, including OCT reflectance and retinal thickness measurements can help to mitigate their effect. Outside of this specific example, OCTA is fortunate in that it is automatically registered with the structural OCT signal. The combination of structural and angiographic information is potent for analyzing and diagnosing pathology (Park et al., 2018).
- (3) **It is often advantageous to design to the volumetric nature of OCTA data.** Appealing to multiple data representations, instead of just *en face* images, can prevent misleading quantification, such as when retinal fluid areas do not accurately reflect the volume of the fluid region (Guo et al., 2020). 3D quantification can also be more precise than an equivalent 2D quantification for certain measurements (Wang et al., 2019). Likely this is in part attributable to the larger amount of information available in volumetric data. But large amounts of irrelevant data can make training deep learning models more difficult-another reason that input selection is important in OCTA analysis.

## 6. Summary

Applying advanced AI-based approaches to OCTA data yields detection and quantification of retinal pathology that would be difficult or impossible to achieve with different methods. Deep-learning-based analysis has already demonstrated parity with human grading in several tasks, even though most networks trained to interpret OCTA have been trained on small datasets. With the growing adoption of OCTA in clinical practice and corresponding increase in the amount of available OCTA data, AI-based analysis only promises to improve. It is likely that AI will continue to provide new insights and capabilities along the way.

## Author statement

All authors have seen this work and contributed as follows:

Tristan T. Hormel: drafting the article

Thomas S. Hwang, Steven T. Bailey, David J. Wilson, David Huang, and Yali Jia: critical review

Yali Jia: conception and content

All relevant disclosures are given below, and will be included in a future manuscript version that includes author details.

## Declaration of competing interest

Oregon Health & Science University (OHSU) and Drs. Jia and Huang have a financial interest in Optovue Inc. OHSU and Dr. Jia also have financial interest in Optos Inc. These potential conflicts of interest have been reviewed and are managed by OHSU. The other authors do not have any potential financial conflicts of interest.

## Acknowledgements

This work was supported by grant National Institutes of Health (R01 EY027833, R01 EY024544, R01EY031394, R01 EY023285, P30 EY010572); Unrestricted Departmental Funding Grant, William & Mary Greve Special Scholar Award from Research to Prevent Blindness (New York, NY) and the Bright Focus Foundation (G2020168). We also thank Acner Camino, Min Gao, Yukun Guo, Jie Wang, Xiang Wei, and Pengxiao Zang for contributing to this work.

## References

- Agemy, S.A., Sripsema, N.K., Shah, C.M., Chui, T., Garcia, P.M., Lee, J.G., Gentile, R.C., Hsiao, Y.S., Zhou, Q., Ko, T., Rosen, R.B., 2015. Retinal vascular perfusion density mapping using optical coherence tomography angiography in normals and diabetic retinopathy patients. *Retina* 35, 2353–2363. <https://doi.org/10.1097/IAE.0000000000000862>.
- Ahlers, C., Simader, C., Geitzenauer, W., Stock, G., Stetson, P., Dastmalchi, S., Schmidt-Erfurth, U., 2008. Automatic segmentation in three-dimensional analysis of fibrovascular pigmentepithelial detachment using high-definition optical coherence tomography. *Br. J. Ophthalmol.* 92, 197–203. <https://doi.org/10.1136/bjo.2007.120956>.
- Al-sheikh, M., Tepelus, T.C., Nazikyan, T., Sadda, S.R.V.R., 2017. Repeatability of automated vessel density measurements using optical coherence tomography angiography. *Br. J. Ophthalmol.* 101, 449–452. <https://doi.org/10.1136/bjophthalmol-2016-308764>.
- Alam, M., 2019. Supervised machine learning based multi-task artificial intelligence classification of retinopathies. *J. Clin. Med.* 8, 872. <https://doi.org/10.3390/jcm8060872>.
- Alam, M., Le, D., Son, T., Lim, J.I., Yao, X., 2020a. AV-Net: deep learning for fully automated artery-vein classification in optical coherence tomography angiography. *Biomed. Opt Express* 11, 5249. <https://doi.org/10.1364/boe.399514>.
- Alam, M., Lim, J.I., Toslak, D., Yao, X., 2019a. Differential artery-vein analysis improves the performance of OCTA staging of sickle cell retinopathy. *Transl. Vis. Sci. Technol.* 8 <https://doi.org/10.1167/tvst.8.2.3>.
- Alam, M., Toslak, D., Lim, J.I., Yao, X., 2019b. OCT feature analysis guided artery-vein differentiation in OCTA. *Biomed. Opt Express* 10, 2055. <https://doi.org/10.1364/boe.10.002055>.
- Alam, M., Toslak, D., Lim, J.I., Yao, X., 2018. Color fundus image guided artery-vein differentiation in optical coherence tomography angiography. *Investig. Ophthalmol. Vis. Sci.* 59, 4953–4962. <https://doi.org/10.1167/iovs.18-24831>.
- Alam, M., Zhang, Y., Lim, J.I., Chan, R.V.P., Yang, M., Yao, X., 2020b. Quantitative optical coherence tomography angiography features for objective classification and staging of diabetic retinopathy. *Retina* 40, 322–332. <https://doi.org/10.1097/IAE.0000000000002373>.
- An, L., Shen, T.T., Wang, R.K., 2011. Using ultrahigh sensitive optical microangiography to achieve comprehensive depth resolved microvasculature mapping for human retina. *J. Biomed. Opt.* 16, 106013. <https://doi.org/10.1117/1.3642638>.
- An, L., Wang, R.K., 2008. In vivo volumetric imaging of vascular perfusion within human retina and choroids with optical micro-angiography. *Opt Express* 16, 11438–11452. <https://doi.org/10.1364/OE.16.011438>.
- Antonetti, D.A., Klein, R., Gardner, T.W., 2012. Diabetic retinopathy. *N. Engl. J. Med.* 366, 1227–1239. [https://doi.org/10.1016/S0140-6736\(09\)62124-3](https://doi.org/10.1016/S0140-6736(09)62124-3).
- Antony, B.J., Abràmoff, M.D., Lee, K., Sonkova, P., Gupta, P., Kwon, Y., Niemeijer, M., Hu, Z., Garvin, M.K., 2010. Automated 3D segmentation of intraretinal layers from optic nerve head optical coherence tomography images. *Med. Imaging 2010 Biomed. Appl. Mol. Struct. Funct. Imaging* 7626, 76260U. <https://doi.org/10.1117/12.843928>.
- Arnould, L., Guenancia, C., Azemar, A., Alan, G., Pitois, S., Bichat, F., Zeller, M., Gabrieille, P.H., Bron, A.M., Creuzot-Garcher, C., Cottin, Y., 2018. The EYE-MI pilot study: a prospective acute coronary syndrome cohort evaluated with retinal optical coherence tomography angiography. *Investig. Ophthalmol. Vis. Sci.* 59, 4299–4306. <https://doi.org/10.1167/iovs.18-24090>.
- Bai, F., Marques, M.J., Gibson, S.J., 2017. Cystoid Macular Edema Segmentation of Optical Coherence Tomography Images Using Fully Convolutional Neural Networks and Fully Connected CRFs. [arXiv](https://arxiv.org/abs/1703.08901).
- Bailey, S.T., Thaware, O., Wang, J., Hagag, A.M., Zhang, X., Flaxel, C.J., Lauer, A.K., Hwang, T.S., Lin, P., Huang, D., Jia, Y., 2019. Detection of nonexudative choroidal neovascularization and progression to exudative choroidal neovascularization using OCT angiography. *Ophthalmol. Retin.* 3, 629–636. <https://doi.org/10.1016/j.oret.2019.03.008>.
- Baroni, M., Fortunato, P., La Torre, A., 2007. Towards quantitative analysis of retinal features in optical coherence tomography. *Med. Eng. Phys.* 29, 432–441. <https://doi.org/10.1016/j.medengphy.2006.06.003>.
- Bhavsar, K.V., Jia, Y., Wang, J., Patel, R.C., Lauer, A.K., Huang, D., Bailey, S.T., 2017. Projection-resolved optical coherence tomography angiography exhibiting early flow prior to clinically observed retinal angiomatic proliferation. *Am. J. Ophthalmol. Case Reports* 8, 53–57. <https://doi.org/10.1016/j.jajoc.2017.10.001>.
- Bishop, C.M., 1995. Neural networks for pattern recognition. In: *Advances in Computers*. Oxford University Press. [https://doi.org/10.1016/S0065-2458\(08\)60404-0](https://doi.org/10.1016/S0065-2458(08)60404-0).
- Braaf, B., Vienna, K.V., Sheehy, C.K., Yang, Q., Vermeer, K.A., Tiruveedhula, P., Arathorn, D.W., Roorda, A., de Boer, J.F., 2013. Real-time eye motion correction in phase-resolved OCT angiography with tracking SLO. *Biomed. Opt Express* 4, 51. <https://doi.org/10.1364/boe.4.000051>.
- Brown, N., Sandholm, T., 2019. Superhuman AI for multiplayer poker. *Science* 84 365, 885–890. <https://doi.org/10.1126/science.aaay2400>.
- Browning, D.J., Glassman, A.R., Aiello, L.P., Bressler, N.M., Bressler, S.B., Danis, R.P., Davis, M.D., Ferris, F.L., Huang, S.S., Kaiser, P.K., Kollman, C., Sadda, S., Scott, I.U., Qin, H., 2008. Optical coherence tomography measurements and analysis methods in optical coherence tomography studies of diabetic macular edema. *Ophthalmology* 115, 1366–1372. <https://doi.org/10.1016/j.joptha.2007.12.004>.
- Buchanan, B.G., Shortliffe, E.H., 1984. *Rule-based Expert Systems : the MYCIN Experiments of the Stanford Heuristic Programming Project*. Addison-Wesley.
- Cabrera Fernández, D., Salinas, H.M., Puliafito, C.A., 2005. Automated detection of retinal layer structures on optical coherence tomography images. *Opt Express* 13, 10200. <https://doi.org/10.1364/oxpre.13.010200>.
- Camino, A., Jia, Y., Liu, G., Wang, J., Huang, D., 2017. Regression-based algorithm for bulk motion subtraction in optical coherence tomography angiography. *Biomed. Opt Express* 8, 3053–3066. <https://doi.org/10.1364/BOE.8.003053>.
- Camino, A., Jia, Y., Yu, J., Wang, J., Liu, L., Huang, D., 2019. Automated detection of shadow artifacts in optical coherence tomography angiography. *Biomed. Opt Express* 10, 1514–1531. <https://doi.org/10.1364/BOE.10.001514>.
- Camino, A., Wang, Z., Wang, J., Pennesi, M.E., Yang, P., Huang, D., Li, D., Jia, Y., 2018a. Deep learning for the segmentation of preserved photoreceptors on en face optical coherence tomography in two inherited retinal diseases. *Biomed. Opt Express* 9, 3092–3105. <https://doi.org/10.1364/BOE.9.003092>.
- Camino, A., Zhang, M., Dongye, C., Pechauer, A.D., Hwang, T.S., Bailey, S.T., Lujan, B., Wilson, D.J., Huang, D., Jia, Y., 2016a. Automated registration and enhanced processing of clinical optical coherence tomography angiography. *Quant. Imag. Med. Surg.* 6, 391–401. <https://doi.org/10.21037/qims.2016.07.02>.
- Camino, A., Zhang, M., Gao, S.S., Hwang, T.S., Sharma, U., Wilson, D.J., Huang, D., Jia, Y., 2016b. Evaluation of artifact reduction in optical coherence tomography angiography with real-time tracking and motion correction technology. *Biomed. Opt Express* 7, 3905–3915. <https://doi.org/10.1364/boe.7.003905>.
- Camino, A., Zhang, M., Liu, L., Wang, J., Jia, Y., Huang, D., 2018b. Enhanced quantification of retinal perfusion by improved discrimination of blood flow from bulk motion signal in OCTA. *Transl. Vis. Sci. Technol.* 7 <https://doi.org/10.1167/tvst.7.6.20>.
- Campbell, J.P., Zhang, M., Hwang, T.S., Bailey, S.T., Wilson, D.J., Jia, Y., Huang, D., 2017. Detailed vascular anatomy of the human retina by projection-resolved optical coherence tomography angiography. *Sci. Rep.* 7, 1–11. <https://doi.org/10.1038/srep42201>.
- Chen, L., Zhang, X., Wen, F., 2018. Venous beading in two or more quadrants might not be a sensitive grading criterion for severe nonproliferative diabetic retinopathy. *Graefes Arch. Clin. Exp. Ophthalmol.* 256, 1059–1065. <https://doi.org/10.1007/s00417-018-3971-3>.

- Chen, Z., Milner, T.E., Srinivas, S., Wang, X., Malekafzali, a, van Gemert, M.J., Nelson, J.S., 1997. Noninvasive imaging of in vivo blood flow velocity using optical Doppler tomography. *Opt. Lett.* 22, 1119–1121. <https://doi.org/10.1364/OL.22.001119>.
- Chidambara, L., Gadde, S.G.K., Yadav, N.K., Jayadev, C., Bhanushali, D., Appaji, A.M., Akkali, M., Khurana, A., Shetty, R., 2016. Characteristics and quantification of vascular changes in macular telangiectasia type 2 on optical coherence tomography angiography. *Br. J. Ophthalmol.* 100, 1482–1488. <https://doi.org/10.1136/bjophthalmol-2015-307941>.
- Chiu, S.J., Allingham, M.J., Mettu, P.S., Cousins, S.W., Izatt, J.A., Farsiu, S., 2015. Kernel regression based segmentation of optical coherence tomography images with diabetic macular edema. *Biomed. Opt Express* 6, 1172–1194. <https://doi.org/10.1364/BOE.6.001172>.
- Chiu, S.J., Li, X.T., Nicholas, P., Toth, C.A., Izatt, J.A., Farsiu, S., 2010. Automatic segmentation of seven retinal layers in SD OCT images congruent with expert manual segmentation. *Opt Express* 18, 19413–19428.. <https://doi.org/10.1364/OE.18.019413>.
- Clebiej, M., Gorcynska, I., Rutkowski, A., Kluczewski, J., Grzona, T., Pijewska, E., Sikorski, B.L., Szkulmowska, A., Szkulmowski, M., 2019. Quality improvement of OCT angiograms with elliptical directional filtering. *Biomed. Opt Express* 10, 1013. <https://doi.org/10.1364/boe.10.001013>.
- Corvi, F., Pellegrini, M., Erba, S., Cozzi, M., Staurenghi, G., Giani, A., 2018. Reproducibility of vessel density, fractal dimension, and foveal avascular zone using 7 different optical coherence tomography angiography devices. *Am. J. Ophthalmol.* 186, 25–31. <https://doi.org/10.1016/j.ajo.2017.11.011>.
- Dai, Q., Sun, Y., 2011. Automated layer segmentation of optical coherence tomography images. *Proc. - 2011 4th Int. Conf. Biomed. Eng. Informatics, BMEI* 1, 142–146. <https://doi.org/10.1109/BMEI.2011.6098329>, 2011.
- Dansingani, K.K., Naysan, J., Freund, K.B., 2015. En face OCT angiography demonstrates flow in early type 3 neovascularization (retinal angiomatic proliferation). *Eye* 29, 703–706. <https://doi.org/10.1038/eye.2015.27>.
- Das, R., Spence, G., Hogg, R.E., Stevenson, M., Chakravarthy, U., 2018. Disorganization of inner retina and outer retinal morphology in diabetic macular edema. *JAMA Ophthalmol* 136, 202–208. <https://doi.org/10.1001/jamaophthalmol.2017.6256>.
- de Oliveira Dias, J.R., Zhang, Q., Garcia, J.M.B., Zheng, F., Motulsky, E.H., Roisman, L., Miller, A., Chen, C.L., Kubach, S., de Sisternes, L., Durbin, M.K., Feuer, W., Wang, R.K., Gregori, G., Rosenfeld, P.J., 2018. Natural history of subclinical neovascularization in nonexudative age-related macular degeneration using swept-source OCT angiography. In: *Ophthalmology*. American Academy of Ophthalmology, pp. 255–266. <https://doi.org/10.1016/j.jophtha.2017.08.030>.
- Deng, J., Dong, W., Socher, R., Li, L.-J., Li, K., Li, F.-F., 2009. ImageNet: a large-scale hierarchical image database. In: *2009 IEEE Conference on Computer Vision and Pattern Recognition*.
- Devalla, S.K., Renukanand, P.K., Sreedhar, B.K., Subramanian, G., Zhang, L., Perera, S., Mari, J.-M., Chin, K.S., Tun, T.A., Strouthidis, N.G., Aung, T., Thiéry, A.H., Girard, M.J.A., 2018. DRUNET: a dilated-residual U-Net deep learning network to segment optic nerve head tissues in optical coherence tomography images. *Biomed. Opt Express* 9, 3244. <https://doi.org/10.1364/boe.9.003244>.
- Diabetic Retinopathy Clinical Research Network, 2008. The relationship between OCT-measured central retinal thickness and visual acuity in diabetic macular edema. *Ophthalmology* 114, 525–536. <https://doi.org/10.1016/j.ophtha.2006.06.052> (The).
- DiCarlo, J.J., Zoccolan, D., Rust, N.C., 2012. How does the brain solve visual object recognition? *Neuron* 73, 415–434. <https://doi.org/10.1016/j.neuron.2012.01.010>.
- Dong, C., Loy, C.C., He, K., Tang, X., 2016. Image super-resolution using deep convolutional networks. *IEEE Trans. Pattern Anal. Mach. Intell.* 38, 295–307. <https://doi.org/10.1109/TPAMI.2015.2439281>.
- Dongye, C., Zhang, M., Hwang, T.S., Wang, J., Gao, S.S., Liu, L., Huang, D., Wilson, D.J., Jia, Y., 2017. Automated detection of dilated capillaries on optical coherence tomography angiography. *Biomed. Opt Express* 8, 1101–1109. <https://doi.org/10.1364/BOE.8.001101>.
- Dufour, P.A., Ceklic, L., Abdillahi, H., Schroder, S., De Dzanet, S., Wolf-Schnurrbusch, U., Kowal, J., 2013. Graph-based multi-surface segmentation of OCT data using trained hard and soft constraints. *IEEE Trans. Med. Imag.* 32, 531–543. <https://doi.org/10.1109/TMI.2012.2225152>.
- Eladawi, N., Elmogy, M., Helmy, O., Aboelfetouh, A., Riad, A., Sandhu, H., Schaaf, S., El-Baz, A., 2017. Automatic blood vessels segmentation based on different retinal maps from OCTA scans. *Comput. Biol. Med.* 89, 150–161. <https://doi.org/10.1016/j.combiomed.2017.08.008>.
- Ester, M., Kriegel, H.-P., Sander, J., Xu, X., 1996. A density-based algorithm for discovering clusters in large spatial databases with noise. *Proc. Second Int. Conf. Knowl. Discov. Data Min.* 635, 226–231. <https://doi.org/10.1016/B978-044452701-1.00067-3>.
- Fabritius, T., Makita, S., Miura, M., Myllylä, R., Yasuno, Y., 2009. Automated segmentation of the macula by optical coherence tomography. *Opt Express* 17, 15659. <https://doi.org/10.1364/oe.17.015659>.
- Fang, L., Cunefare, D., Wang, C., Guymer, R.H., Li, S., Farsiu, S., 2017. Automatic segmentation of nine retinal layer boundaries in OCT images of non-exudative AMD patients using deep learning and graph search. *Biomed. Opt Express* 8, 2732. <https://doi.org/10.1364/boe.8.002732>.
- Ferguson, R.D., Hammer, D.X., Paunescu, L.A., Beaton, S., Schuman, J.S., 2004. Tracking optical coherence tomography. *Opt. Lett.* 29, 2139–2141. <https://doi.org/10.1038/jid.2014.371>.
- Flaxman, S.R., Bourne, R.R.A., Resnikoff, S., Ackland, P., Braithwaite, T., Cincinelli, M.V., Das, A., Jonas, J.B., Keeffe, J., Kempen, J., Leasher, J., Limburg, H., Naidoo, K., Pesudovs, K., Silvester, A., Stevens, G.A., Tahhan, N., Wong, T., Taylor, H., Ardit, A., Barkana, Y., Bozkurt, B., Bron, A., Budenz, D., Cai, F., Casson, R., Chakravarthy, U., Choi, J., Congdon, N., Dana, R., Dandona, R., Dandona, L., Dekaris, I., Del Monte, M., Deva, J., Dreer, L., Ellwein, L., Frazier, M., Frick, K., Friedman, D., Furtado, J., Gao, H., Gazzard, G., George, R., Gichuhi, S., Gonzalez, V., Hammond, B., Hartnett, M.E., He, M., Hejtmancik, J., Hirai, F., Huang, J., Ingram, A., Javitt, J., Joslin, C., Khairallah, M., Khanna, R., Kim, J., Lambrou, G., Lanssing, V.C., Lanzetta, P., Lim, J., Mansouri, K., Mathew, A., Morse, A., Munoz, B., Musch, D., Nangia, V., Palaiou, M., Parodi, M.B., Pena, F.Y., Petto, T., Quigley, H., Raju, M., Ramulu, P., Reza, D., Robin, A., Rossetti, L., Saadine, J., Sandar, M., Serle, J., Shen, T., Shetty, R., Sieving, P., Silva, J.C., Sitorus, R.S., Stambolian, D., Tejedor, J., Tielsch, J., Tsilimbaris, M., van Meurs, J., Varma, R., Virgili, G., Wang, Y.X., Wang, N.L., West, S., Wiedemann, P., Wormald, R., Zheng, Y., 2017. Global causes of blindness and distance vision impairment 1990–2020: a systematic review and meta-analysis. *Lancet Glob. Health* 5, e1221–e1234. [https://doi.org/10.1016/S2214-109X\(17\)30393-5](https://doi.org/10.1016/S2214-109X(17)30393-5).
- Frangi, A.F., Niessen, W.J., Vincken, K.L., Viergever, M.A., 1998. Multiscale Vessel Enhancement Filtering 1496, 130–137. <https://doi.org/10.1007/BFb0056195>.
- Fujimoto, J., Swanson, E., 2016. The development, commercialization, and impact of optical coherence tomography. *Investig. Ophthalmol. Vis. Sci.* 57, OCT1–OCT13. <https://doi.org/10.1167/iosv.16-19963>.
- Fukushima, K., 1980. Neocognitron: a self-organizing neural network model for a mechanism of pattern recognition unaffected by shift in position. *Biol. Cybern.* 36, 193–202. <https://doi.org/10.1007/BF00344251>.
- Gao, M., Guo, Y., Hormel, T.T., Sun, J., Hwang, T.S., Jia, Y., 2020. Reconstruction of high-resolution 6×6-mm OCT angiograms using deep learning. *Biomed. Opt Express* 11, 3585. <https://doi.org/10.1364/boe.394301>.
- Gao, S.S., Jia, Y., Liu, L., Zhang, M., Takasugawa, H.L., Morrison, J.C., Huang, D., 2016a. Compensation for reflectance variation in vessel density quantification by optical coherence tomography angiography. *Investig. Ophthalmol. Vis. Sci.* 57, 4485–4492. <https://doi.org/10.1167/iosv.16-20080>.
- Gao, S.S., Jia, Y., Zhang, M., Su, J.P., Liu, G., Hwang, T.S., Bailey, S.T., Huang, D., 2016b. Optical coherence tomography angiography. *Investig. Ophthalmol. Vis. Sci.* 57, OCT27–OCT36. <https://doi.org/10.1167/iosv.15-19043>.
- Gao, S.S., Liu, G., Huang, D., Jia, Y., 2015. Optimization of the split-spectrum amplitude-decorrelation angiography algorithm on a spectral optical coherence tomography system. *Opt. Lett.* 40, 2305–2308. <https://doi.org/10.1364/OL.40.002305>.
- Gao, S.S., Patel, R.C., Jain, N., Zhang, M., Weleber, R.G., Huang, D., Pennesi, M.E., 2017a. Choriocapillary evaluation in choroideeritis using optical coherence tomography angiography. *Biomed. Opt Express* 8, 48–56.
- Gao, Z., Bu, W., Zheng, Y., Wu, X., 2017b. Automated layer segmentation of macular OCT images via graph-based SLIC superpixels and manifold ranking approach. *Comput. Med. Imag. Graph.* 55, 42–53. <https://doi.org/10.1016/j.compmedimag.2016.07.006>.
- Gao, E., Shi, F., Zhu, W., Jin, C., Sun, M., Chen, H., Chen, X., 2017c. Graph search: active appearance model based automated segmentation of retinal layers for optic nerve head centered OCT images. *Med. Imaging 2017 Image Process* 10133, 101331Q. <https://doi.org/10.1117/12.2250168>.
- Garvin, M.K., Abràmoff, M.D., Kardon, R.H., Russell, S.R., Wu, X., Sonka, M., 2008. Intraretinal layer segmentation of macular OCT images using optimal 3D graph search. *IEEE Trans. Med. Imag.* 27, 1495–1505. <https://doi.org/10.1109/TMI.2008.923966>.
- Goodfellow, I.J., Bengio, Y., Courville, A., 2016. Deep Learning. Deep Learning. The MIT Press.
- Goodfellow, I.J., Pouget-Abadie, J., Mirza, M., Xu, B., Warde-Farley, D., Ozair, S., Courville, A., Bengio, 2014. Generative adversarial nets. Advances in Neural Information Processing Systems.
- Gopinath, K., Sivaswamy, J., 2019. Segmentation of retinal cysts from optical coherence tomography volumes via selective enhancement. *IEEE J. Biomed. Heal. Informatics* 23, 273–282. <https://doi.org/10.1109/JBHI.2018.2793534>.
- Guo, Y., Camino, A., Wang, J., Huang, D., Hwang, T.S., Jia, Y., 2018a. MEDnet, a neural network for automated detection of avascular area in OCT angiography. *Biomed. Opt Express* 9, 5147–5158. <https://doi.org/10.1364/BOE.9.005147>.
- Guo, Y., Camino, A., Zhang, M., Wang, J., Huang, D., Hwang, T., Jia, Y., 2018b. Automated segmentation of retinal layer boundaries and capillary plexuses in wide-field optical coherence tomographic angiography. *Biomed. Opt Express* 9, 4429–4442. <https://doi.org/10.1364/BOE.9.004429>.
- Guo, Y., Hormel, T.T., Xiong, H., Wang, B., Camino, A., Wang, J., Huang, D., Hwang, T.S., Jia, Y., 2019. Development and validation of a deep learning algorithm for distinguishing the nonperfusion area from signal reduction artifacts on OCT angiography. *Biomed. Opt Express* 10, 3257. <https://doi.org/10.1364/boe.10.003257>.
- Guo, Y., Hormel, T.T., Xiong, H., Wang, J., Hwang, T.S., Jia, Y., 2020. Automated Segmentation of Retinal Fluid Volumes from Structural and Angiographic Optical Coherence Tomography Using Deep Learning.
- Haeker, M., Sonka, M., Kardon, R., Shah, V.A., Wu, X., Abràmoff, M.D., 2007. Automated segmentation of intraretinal layers from macular optical coherence tomography images. *Med. Imaging 2007 Image Process* 6512, 651214. <https://doi.org/10.1117/12.710231>.
- He, K., Zhang, X., Ren, S., Sun, J., 2016. Deep residual learning for image recognition. *Proc. IEEE Comput. Soc. Conf. Comput. Vis. Pattern Recognit.* 2016-Decem 770–778. <https://doi.org/10.1109/CVPR.2016.90>.
- Heiferman, M.J., Fawzi, A.A., 2019. Progression of subclinical choroidal neovascularization in age-related macular degeneration. *PloS One* 14, 1–9. <https://doi.org/10.1371/journal.pone.0217805>.
- Heisler, M., Chan, F., Mammo, Z., Balaratnasingam, C., Prentasic, P., Docherty, G., Ju, M., Rajapakse, S., Lee, S., Merkur, A., Kirker, A., Albiani, D., Maberley, D., Freund, K.B., Beg, M.F., Loncaric, S., Sarunic, M.V., Navajas, E.V., 2019. Deep

- Learning Vessel Segmentation and Quantification of the Foveal Avascular Zone Using Commercial and Prototype OCT-A Platforms.** arXiv.
- Heisler, M., Karst, S., Lo, J., Mammo, Z., Yu, T., Warner, S., Maberley, D., Beg, M.F., Navajas, E.V., Sarunic, M.V., 2020a. Ensemble deep learning for diabetic retinopathy detection using optical coherence tomography angiography. *Transl. Vis. Sci. Technol.* 9, 20. <https://doi.org/10.1167/tvst.9.2.20>.
- Heisler, M., Karst, S., Lo, J., Mammo, Z., Yu, T., Warner, S., Maberley, D., Beg, M.F., Navajas, E.V., Sarunic, M.V., 2020b. Ensemble deep learning for diabetic retinopathy detection using optical coherence tomography angiography. *Transl. Vis. Sci. Technol.* 9, 1–11. <https://doi.org/10.1167/tvst.9.2.20>.
- Hendargo, H.C., Estrada, R., Chiu, S.J., Tomasi, C., Farsiu, S., Izatt, J.A., 2013. Automated non-rigid registration and mosaicing for robust imaging of distinct retinal capillary beds using speckle variance optical coherence tomography. *Biomed. Opt Express* 4, 803. <https://doi.org/10.1364/boe.4.000803>.
- Holmen, I.C., Konda, M.S., Pak, J.W., McDaniel, K.W., Blodi, B., Stepien, K.E., Domalpally, A., 2019. Prevalence and severity of artifacts in optical coherence tomographic angiograms. *JAMA Ophthalmol* 137(17), 119–126. <https://doi.org/10.1001/jamaophthalmol.2019.4971>.
- Hood, D.C., Kardon, R.H., 2007. A framework for comparing structural and functional measures of glaucomatous damage. *Prog. Retin. Eye Res.* <https://doi.org/10.1016/j.preteyes.2007.08.001>.
- Hormel, T.T., Jia, Y., Jian, Y., Hwang, T.S., Bailey, S.T., Pennesi, M.E., Wilson, D.J., Morrison, J.C., Huang, D., 2020. Plexus-specific retinal vascular anatomy and pathologies as seen by projection-resolved optical coherence tomographic angiography. *Prog. Retin. Eye Res.* 100878. <https://doi.org/10.1016/j.preteyes.2020.100878>.
- Hormel, T.T., Wang, J., Bailey, S.T., Hwang, T.S., Huang, D., Jia, Y., 2018. Maximum value projection produces better en face OCT angiograms than mean value projection. *Biomed. Opt Express* 9, 6412–6424. <https://doi.org/10.1364/BOE.9.006412>.
- Hossbach, J., Husvogt, L., Kraus, M.F., Fujimoto, J.G., Maier, A.K., 2020. Deep OCT angiography image generation for motion artifact suppression. arXiv. [https://doi.org/10.1107/978-3-658-29267-6\\_55](https://doi.org/10.1107/978-3-658-29267-6_55).
- Huang, D., Swanson, E.A., Lin, C.P., Schuman, J.S., Stinson, W.G., Chang, W., Hee, M.R., Flotte, T., Gregory, K., Puliafito, C.A., Fujimoto, J.G., 1991. Optical coherence tomography. *Science* 242, 1178–1181. <https://doi.org/10.1126/science.24872> (The).
- Hubel, D.H., Wiesel, T.N., 1968. Receptive fields and functional architecture of monkey striate cortex. *J. Physiol.* 195, 215–243. <https://doi.org/10.1113/jphysiol.1968.sp008455>.
- Hubel, D.H., Wiesel, T.N., 1959. Receptive fields of single neurones in the cat's striate cortex. *J. Physiol.* 148, 574–591. <https://doi.org/10.1109/SOCC.2011.6085109>.
- Hwang, T.S., Gao, S.S., Liu, L., Lauer, A.K., Bailey, S.T., Flaxel, C.J., Wilson, D.J., Huang, D., Jia, Y., 2016. Automated quantification of capillary nonperfusion using optical coherence tomography angiography in diabetic retinopathy. *JAMA Ophthalmol* 134, 367–373. <https://doi.org/10.1001/jamaophthalmol.2015.5658>.
- Hyvärinen, A., Hurri, J., Hoyer, P.O., 2009. Natural Image Statistics A Probabilistic Approach to Early Computational Vision, Springer-Verlag. <https://doi.org/10.1007/BF02188754>.
- Ishibazawa, A., Nagaoka, T., Takahashi, A., Omae, T., Tani, T., Sogawa, K., Yokota, H., Yoshida, A., 2015. Optical coherence tomography angiography in diabetic retinopathy: a prospective pilot study. *Am. J. Ophthalmol.* 160, 35–44. [https://doi.org/10.1016/j.ajo.2015.04.021 e1](https://doi.org/10.1016/j.ajo.2015.04.021).
- Ishikawa, H., Stein, D.M., Wollstein, G., Beaton, S., Fujimoto, J.G., Schuman, J.S., 2005. Macular segmentation with optical coherence tomography. *Investig. Ophthalmol. Vis. Sci.* 46, 2012–2017. <https://doi.org/10.1167/iovs.04-0335>.
- Isola, P., Zhu, J.Y., Zhou, T., Efros, A.A., 2017. Image-to-image translation with conditional adversarial networks. In: Proc. - 30th IEEE Conf. Comput. Vis. Pattern Recognition, CVPR 2017 2017-Janua, p. 5967. <https://doi.org/10.1109/CVPR.2017.632>.
- Izatt, J.A., Kulkarni, M.D., Yazdanfar, S., Barton, J.K., Welch, A.J., 1997. In vivo bidirectional color Doppler flow imaging of picoliter blood volumes using optical coherence tomography. *Opt. Lett.* 22, 1439–1441. <https://doi.org/10.1364/OL.22.001439>.
- Janocha, K., Czarnecki, W.M., 2017. On Loss Functions for Deep Neural Networks in Classification. arXiv. <https://doi.org/10.4467/20838476SI.16.004.6185>.
- Jarrett, K., Kavukcuoglu, K., Ranzato, M., LeCun, Y., 2009. What is the best multi-stage architecture for object recognition? *Proc. IEEE Int. Conf. Comput. Vis.* 2146–2153. <https://doi.org/10.1109/ICCV.2009.5459469>.
- Jenkins, A.J., Joglekar, M.V., Hardikar, A.A., Keech, A.C., O'Neal, D.N., Januszewski, A. S., 2015. Biomarkers in diabetic retinopathy. *Rev. Diabet. Stud.* 12, 159–195. <https://doi.org/10.1900/RDS.2015.12.159>.
- Jia, Y., Bailey, S.T., Hwang, T.S., McLintic, S.M., Gao, S.S., Pennesi, M.E., Flaxel, C.J., Lauer, A.K., Wilson, D.J., Horngger, J., Fujimoto, J.G., Huang, D., 2015. Quantitative optical coherence tomography angiography of vascular abnormalities in the living human eye. *Proc. Natl. Acad. Sci. U. S. A.* 112, E2395–E2402. <https://doi.org/10.1073/pnas.1500185112>.
- Jia, Y., Bailey, S.T., Wilson, D.J., Tan, O., Klein, M.L., Flaxel, C.J., Potsaid, B., Liu, J.J., Lu, C.D., Kraus, M.F., Fujimoto, J.G., Huang, D., 2014a. Quantitative optical coherence tomography angiography of choroidal neovascularization in age-related macular degeneration. *Ophthalmology* 121, 1435–1444. <https://doi.org/10.1016/j.ophtha.2014.01.034>.
- Jia, Y., Tan, O., Tokayer, J., Potsaid, B., Wang, Y., Liu, J.J., Kraus, M.F., Subhash, H., Fujimoto, J.G., Horngger, J., Huang, D., 2012. Split-spectrum amplitude-decoration angiography with optical coherence tomography. *Opt Express* 20, 4710–4725. <https://doi.org/10.1364/OE.20.004710>.
- Jia, Y., Wei, E., Wang, X., Zhang, X., Morrison, J.C., Parikh, M., Lombardi, L.H., Gatney, D.M., Armour, R.L., Edmunds, B., Kraus, M.F., Fujimoto, J.G., Huang, D., 2014b. Optical coherence tomography angiography of optic disc perfusion in glaucoma. *Ophthalmology* 121, 1322–1332. <https://doi.org/10.1016/j.ophtha.2014.01.021>.
- Jiang, Z., Huang, Z., Qiu, B., Meng, X., You, Y., Liu, X., Geng, M., Liu, G., 2020a. Weakly supervised deep learning based optical coherence tomography angiography. *IEEE Trans. Med. Imag.* 1–11. <https://doi.org/10.1109/TMI.2020.3035154>.
- Jiang, Z., Huang, Z., Qiu, B., Meng, X., You, Y., Liu, X., Liu, G., Zhou, C., Yang, K., Maier, A., Ren, Q., Lu, Y., 2020b. Comparative study of deep learning models for optical coherence tomography angiography. *Biomed. Opt Express* 11, 1580. <https://doi.org/10.1364/boe.387807>.
- Jolliffe, I.T., 2002. *Principle Component Analysis*, second ed. Springer, New York.
- Kafieh, R., Rabbani, H., Abramoff, M.D., Sonka, M., 2013. Intra-retinal layer segmentation of 3D optical coherence tomography using coarse grained diffusion map. *Med. Image Anal.* 17, 907–928. <https://doi.org/10.1016/j.media.2013.05.006>.
- Karlsson, A., He, J., Swartling, J., Andersson-Engels, S., 2005. Numerical simulations of light scattering by red blood cells. *IEEE Trans. Biomed. Eng.* 52, 13–18. <https://doi.org/10.1109/TBME.2004.839634>.
- Karri, S.P.K., Chakrabarti, D., Chatterjee, J., 2016. Learning layer-specific edges for segmenting retinal layers with large deformations. *Biomed. Opt Express* 7, 2888. <https://doi.org/10.1364/boe.7.002888>.
- Kass, M., Witkin, A., Terzopoulos, D., 1988. Snakes: active contour models. *Int. J. Comput. Vis.* 1, 321–331. <https://doi.org/10.1007/BF00133570>.
- Khan, S.M., Liu, X., Nath, S., Korot, E., Faes, L., Wagner, S.K., Keane, P.A., Sebire, N.J., Burton, M.J., 2020. A global review of publicly available datasets for ophthalmological imaging : barriers to access , usability , and generalisability. *Lancet Digit. Heal.* 3, e51–e66. [https://doi.org/10.1016/S2589-7500\(20\)30240-5](https://doi.org/10.1016/S2589-7500(20)30240-5).
- Kim, J., Lee, J.K., Lee, K.M., 2016. Accurate image super-resolution using very deep convolutional networks. *Proc. IEEE Comput. Soc. Conf. Comput. Vis. Pattern Recognit.* 2016-Decem 1646–1654. <https://doi.org/10.1109/CVPR.2016.182>.
- Klein, R., Klein, B.E.K., Moss, S.E., 2012. Hypertension and retinopathy, arteriolar nicking in a narrowing, and arteriovenous population. *Epidemiol. Biostat.* 112, 92–98.
- Klein, S., Staring, M., Murphy, K., Viergever, M.A., Pluim, J.P.W., 2010. Elastix: a toolbox for intensity-based medical image registration. *IEEE Trans. Med. Imag.* 29, 196–205. <https://doi.org/10.1109/TMI.2009.2035616>.
- Klette, R., 2014. *Concise Computer Vision - An Introduction into Theory and Algorithms*. Springer, London.
- Kraus, M.F., Liu, J.J., Schottenhamml, J., Chen, C.-L., Budai, A., Branchini, L., Ko, T., Ishikawa, H., Wollstein, G., Schuman, J., Duker, J.S., Fujimoto, J.G., Horngger, J., 2014. Quantitative 3D-OCT motion correction with tilt and illumination correction, robust similarity measure and regularization. *Biomed. Opt Express* 5, 2591. <https://doi.org/10.1364/boe.5.002591>.
- Kraus, M.F., Potsaid, B., Mayer, M.A., Bock, R., Baumann, B., Liu, J.J., Horngger, J., Fujimoto, J.G., 2012. Motion correction in optical coherence tomography volumes on a per A-scan basis using orthogonal scan patterns. *Biomed. Opt Express* 3, 1182–1199. <https://doi.org/10.1364/BOE.3.001182>.
- Krizhevsky, A., Sutskever, I., Hinton, G.E., 2012. ImageNet classification with deep convolutional neural networks. *Adv. Neural Inf. Process. Syst.* 1097–1105. <https://doi.org/10.1201/9781420010749>.
- Kugelman, J., Alonso-Caneiro, D., Read, S.A., Vincent, S.J., Collins, M.J., 2018. Automatic segmentation of OCT retinal boundaries using recurrent neural networks and graph search. *Biomed. Opt Express* 9, 5759. <https://doi.org/10.1364/boe.9.005759>.
- Le, D., Alam, M., Yao, C., Lim, J.I., Chan, R.V.P., Toslak, D., Yao, X., 2019. Transfer Learning for Automated OCTA Detection of Diabetic Retinopathy 1–20.
- Le, Q.V., Ngiam, J., Coates, A., Lahiri, A., Prochnow, B., Ng, A.Y., 2011. On optimization methods for deep learning. *Proc. 28th Int. Conf. Mach. Learn.* <https://doi.org/10.1109/ESSCIRC.2016.7598259>.
- Leal, I., Tan, S.Z., Aslam, T., Steeples, L.R., Jones, N.P., Chhabra, R., 2020. Intra and inter-rater agreement of inflammatory choroidal neovascular membrane measurements using optical coherence tomography angiography. *Graefe's Arch. Clin. Exp. Ophthalmol.* 258, 647–651. <https://doi.org/10.1007/s00417-019-04538-1>.
- Lee, C., Cheng, H., Chang, F., Wang, A., 2019a. Optical coherence tomography angiography evaluation of retinal microvasculature before and after carotid angioplasty and stenting. *Sci. Rep.* 1–8. <https://doi.org/10.1038/s41598-019-51382-8>.
- Lee, C.S., Tyring, A.J., Wu, Y., Xiao, S., Rokem, A.S., DeRuyter, N.P., Zhang, Q., Tufail, A., Wang, R.K., Lee, A.Y., 2019b. Generating retinal flow maps from structural optical coherence tomography with artificial intelligence. *Sci. Rep.* 9, 1–11. <https://doi.org/10.1038/s41598-019-42042-y>.
- Lee, C.S.C.S., Tyring, A.J.A., Deruyter, N.P.N.P., Wu, Y., Rokem, A., Lee, A.Y.A.Y., Lee, C.S.C.S., Deruyter, N.P.N.P., Rokem, A., Wu, Y., Lee, A.Y.A.Y., 2017. Deep-learning based, automated segmentation of macular edema in optical coherence tomography. *Biomed. Opt Express* 8, 3440–3448. <https://doi.org/10.1364/boe.8.003440>.
- Lei, J., Al-Sheikh, M., Sadda, S.R., Uji, A., Baghdasaryan, E., Balasubramanian, S., 2017a. Impact of multiple en face image averaging on quantitative assessment from optical coherence tomography angiography images. *Ophthalmology* 124, 944–952. <https://doi.org/10.1016/j.jophtha.2017.02.006>.
- Lei, J., Durbin, M.K., Shi, Y., Uji, A., Balasubramanian, S., Baghdasaryan, E., Al-Sheikh, M., Sadda, S.R., 2017b. Repeatability and reproducibility of superficial macular retinal vessel density measurements using optical coherence tomography

- angiography en face images. *JAMA Ophthalmol* 135, 1092–1098. <https://doi.org/10.1001/jamaophthalmol.2017.3431>.
- Li, M., Chen, Y., Ji, Z., Xie, K., Yuan, S., Chen, Q., Li, S., 2020a. Image projection network: 3D to 2D image segmentation in OCTA images. *IEEE Trans. Med. Imag.* 39, 3343–3354. <https://doi.org/10.1109/TMI.2020.2992244>.
- Li, P.L., O’Neil, C., Saberi, S., Sinder, K., Wang, K.X., Tan, B., Hosseinaee, Z., Bizheva, K., Lakshminarayanan, V., 2020b. Deep learning algorithm for generating optical coherence tomography angiography (OCTA) maps of the retinal vasculature. *Conf. Proc. SPIE* 1151109, 8. <https://doi.org/10.1117/12.2568629>.
- Li, Pei, Cheng, Y., Zhou, L., Pan, C., Ding, Z., Li, Peng, 2016. Single-shot angular compounded optical coherence tomography angiography by splitting full-space B-scan modulation spectrum for flow contrast enhancement. *Opt. Lett.* 41, 1058. <https://doi.org/10.1364/ol.41.001058>.
- Litjens, G., Kooi, T., Bejnordi, B.E., Setio, A.A.A., Ciompi, F., Ghafoorian, M., van der Laak, J.A.W.M., van Ginneken, B., Sánchez, C.I., 2017. A survey on deep learning in medical image analysis. *Med. Image Anal.* 42, 60–88. <https://doi.org/10.1016/j.media.2017.07.005>.
- Liu, G., Jia, Y., Pechauer, A.D., Chandwani, R., Huang, D., 2016. Split-spectrum phase-gradient optical coherence tomography angiography. *Biomed. Opt Express* 7, 2943–2954.
- Liu, L., Gao, S.S., Bailey, S.T., Huang, D., Li, D., Jia, Y., 2015. Automated choroidal neovascularization detection algorithm for optical coherence tomography angiography. *Biomed. Opt Express* 6, 3564–3575. <https://doi.org/10.1364/BOE.6.003564>.
- Liu, Xiaoxiao, Bi, L., Xu, Y., Feng, D., Kim, J., Xu, X., 2019a. Robust deep learning method for choroidal vessel segmentation on swept source optical coherence tomography images. *Biomed. Opt Express* 10, 1601. <https://doi.org/10.1364/boe.10.001601>.
- Liu, Xi, Huang, Z., Wang, Z., Wen, C., Jiang, Z., Yu, Z., Liu, J., Liu, G., Huang, X., Maier, A., Ren, Q., Lu, Y., 2019b. A deep learning based pipeline for optical coherence tomography angiography. *J. Biophot.* 12, 1–10. <https://doi.org/10.1002/jbio.201900008>.
- Liu, X., Kirby, M., Zhao, F., 2014. Motion analysis and removal in intensity variation based OCT angiography. *Biomed. Opt Express* 5, 3833. <https://doi.org/10.1364/boe.5.003833>.
- Lowe, D.G., 1999. Object recognition from local scale-invariant features. *Proc. Int. Conf. Comput. Vis.* [https://doi.org/10.1130/2011.2482\(04](https://doi.org/10.1130/2011.2482(04).
- Lu, D., Heisler, M., Lee, S., Ding, G., Sarunic, M.V., Beg, M.F., 2017. Retinal Fluid Segmentation and Detection in Optical Coherence Tomography Images Using Fully Convolutional Neural Network. *arXiv*. <https://doi.org/10.1117/1.JBO.21.7.075008>.
- Lu, J.Q., Yang, P., Hu, X.-H., 2005. Simulations of light scattering from a biconcave red blood cell using the finite-difference time-domain method. *J. Biomed. Opt.* 10, 024022 <https://doi.org/10.1117/1.1897397>.
- Lu, Y., Simonett, J.M., Wang, J., Zhang, M., Hwang, T., Hagag, A.M., Huang, D., Li, D., Jia, Y., 2018. Evaluation of automatically quantified foveal avascular zone metrics for diagnosis of diabetic retinopathy using optical coherence tomography angiography. *Investig. Ophthalmol. Vis. Sci.* 59, 2212–2221. <https://doi.org/10.1167/iosv.17-23498>.
- Ma, Y., Chen, X., Zhu, W., Cheng, X., Xiang, D., Shi, F., 2018. Speckle noise reduction in optical coherence tomography images based on edge-sensitive cGAN. *Biomed. Opt Express* 9, 5129. <https://doi.org/10.1364/boe.9.0005129>.
- Ma, Y., Hao, H., Xie, J., Fu, H., Zhang, J., Yang, J., Wang, Z., Liu, J., Zheng, Y., Zhao, Y., 2020. ROSE: a retinal OCT-angiography vessel segmentation dataset and new model. *IEEE Trans. Med. Imag.* 40, 928–939. <https://doi.org/10.1109/TMI.2020.3042802>.
- Makita, S., Hong, Y., Yamanari, M., Yatagai, T., Yasuno, Y., 2006. Optical coherence angiography. *Opt Express* 14, 7821–7840. <https://doi.org/10.1364/OE.14.007821>.
- Mariampillai, A., Leung, M.K.K., Jarvi, M., Standish, B.A., Lee, K., Wilson, B.C., Vitkin, A., Yang, V.X.D., 2010. Optimized speckle variance OCT imaging of microvasculature. *Opt. Lett.* 35, 1257–1259. <https://doi.org/10.1364/OL.35.001257>.
- Mariampillai, A., Standish, B.A., Moriyama, E.H., Khurana, M., Munce, N.R., Leung, M.K. K., Jiang, J., Cable, A., Wilson, B.C., Vitkin, I.A., Yang, V.X.D., 2008. Speckle variance detection of microvasculature using swept-source optical coherence tomography. *Opt. Lett.* 33, 1530–1532. <https://doi.org/10.1364/OL.33.001530>.
- Maruko, I., Iida, T., 2016. Polypoidal choroidal vasculopathy. *Surv. Ophthalmol.* 49, 205–215. [https://doi.org/10.1007/978-81-322-3610-8\\_16](https://doi.org/10.1007/978-81-322-3610-8_16).
- Minvielle, W., Caillaux, V., Cohen, S.Y., Chasset, F., Zambrowski, O., Miere, A., Souied, E.H., 2016. Macular microangiopathy in sickle cell disease using optical coherence tomography angiography. *Am. J. Ophthalmol.* 164, 137–144. [https://doi.org/10.1016/j.ajo.2015.12.023 e1](https://doi.org/10.1016/j.ajo.2015.12.023).
- Miri, M.S., Abramoff, M.D., Lee, K., Niemeijer, M., Wang, J.K., Kwon, Y.H., Garvin, M.K., 2015. Multimodal segmentation of optic disc and cup from SD-OCT and color fundus photographs using a machine-learning graph-based approach. *IEEE Trans. Med. Imag.* 34, 1854–1866. <https://doi.org/10.1109/TMI.2015.2412881>.
- Mishra, A., Wong, A., Bizheva, K., Clausi, D.A., 2009. Intra-retinal layer segmentation in optical coherence tomography images. *Opt Express* 17, 23719. <https://doi.org/10.1364/oe.17.023719>.
- Mitchell, P., Liew, G., Gopinath, B., Wong, T.Y., 2018. Age-related macular degeneration. *Lancet* 392, 1147–1159. [https://doi.org/10.1016/S0140-6736\(18\)31550-2](https://doi.org/10.1016/S0140-6736(18)31550-2).
- Montuoro, A., Waldstein, S.M., Gerendas, B.S., Erfurth, U.S., 2017. Joint retinal layer and fluid segmentation in OCT scans of eyes with severe macular edema using unsupervised representation and auto-context. *Biomed. Opt Express* 8, 182–190. <https://doi.org/10.1364/BOE.8.001874>.
- Mujat, M., Chan, R.C., Cense, B., Hyle Park, B., Joo, C., Akkin, T., Chen, T.C., de Boer, J. F., 2005. Retinal nerve fiber layer thickness map determined from optical coherence tomography images. *Opt Express* 13, 9480. <https://doi.org/10.1364/opex.13.009480>.
- Nassif, A.B., Shahin, I., Attili, I., Azzeb, M., Shaalan, K., 2019. Speech recognition using deep neural networks: a systematic review. *IEEE Access* 7, 19143–19165. <https://doi.org/10.1109/ACCESS.2019.2896880>.
- Nesper, P.L., Roberts, P.K., Onishi, A.C., Chai, H., Liu, L., Jampol, L.M., Fawzi, A.A., 2017. Quantifying microvascular abnormalities with increasing severity of diabetic retinopathy using optical coherence tomography angiography. *Investig. Ophthalmol. Vis. Sci.* 58, BIO307–BIO315. <https://doi.org/10.1167/iosv.17-21787>.
- Nesper, P.L., Soetikno, B.T., Treister, A.D., Fawzi, A.A., 2018. Volume-rendered projection-resolved OCT angiography: 3D lesion complexity is associated with therapy response in wet age-related macular degeneration. *Investig. Ophthalmol. Vis. Sci.* 59, 1944–1952. <https://doi.org/10.1167/iosv.17-23361>.
- Niki, T., Muraoka, K., Shimizu, K., 1984. Distribution of capillary nonperfusion in early-stage diabetic retinopathy. *Ophthalmology* 91, 1431–1439. [https://doi.org/10.1016/S0161-6420\(84\)34126-4](https://doi.org/10.1016/S0161-6420(84)34126-4).
- Otsu, N., 1979. A threshold selection method from gray-level histograms. *IEEE Trans. Syst. Man Cybern* 9, 62–66.
- Park, K., Kim, J., Lee, J., 2018. Macular vessel density and ganglion cell/inner plexiform layer thickness and their combinational index using artificial intelligence. *J. Glaucoma* 27, 750–760. <https://doi.org/10.1097/JIG.0000000000000128>.
- Patel, R.C., Wang, J., Hwang, T.S., Zhang, M., Gao, S.S., Pennesi, M.E., Bailey, S.T., Lujan, B.J., Wang, X., Wilson, D.J., Huang, D., Jia, Y., 2018. Plexus-specific detection of retinal vascular pathologic conditions with projection-resolved OCT angiography. *Ophthalmol. Retin.* 2, 816–826. <https://doi.org/10.1016/j.joret.2017.11.010>.
- Pekala, M., Joshi, N., Freund, D.E., Bressler, N.M., DeBuc, D.C., Burlina, P.M., 2018. Deep Learning Based Retinal OCT Segmentation. *arXiv*.
- Pircher, M., Götzinger, E., Leitgeb, R., Fercher, A.F., Hitzenberger, C.K., 2003. Speckle reduction in optical coherence tomography by frequency compounding. *J. Biomed. Opt.* 8, 565. <https://doi.org/10.1117/1.1578087>.
- Popescu, D.P., Choo-Smith, L.P. in, Fluerau, C., Mao, Y., Chang, S., Disano, J., Sherif, S., Sowa, M.G., 2011. Optical coherence tomography: fundamental principles, instrumental designs and biomedical applications. *Biophys. Rev.* 3, 155–169. <https://doi.org/10.1007/s12551-011-0054-7>.
- Prager, S., Sarangi, R., Aiello, L.P., Lammer, J., Silva, P.S., Lin, M.M., Sun, J.K., 2014. Disorganization of the retinal inner layers as a predictor of visual acuity in eyes with center-involved diabetic macular edema. *JAMA Ophthalmol* 132, 1309–1316. <https://doi.org/10.1001/jamaophthalmol.2014.2350>.
- Prentasic, P., Heisler, M., Mammo, Z., Lee, S., Merkur, A., Navajas, E., Beg, M.F., Sarunic, M., Loncaric, S., 2016. Segmentation of the foveal microvasculature using deep learning networks. *J. Biomed. Opt.* 21, 075008 <https://doi.org/10.1117/1.jbo.21.7.075008>.
- Rabiolo, A., Gelormini, F., Sacconi, R., Cicinelli, M.V., Triolo, G., Bettin, P., Nouri-Mahdavi, K., Bandello, F., Querques, G., 2018. Comparison of methods to quantify macular and peripapillary vessel density in optical coherence tomography angiography. *PLoS One* 1–20.
- Rawat, W., Wang, Z., 2017. Deep convolutional neural networks for image classification: a comprehensive review. *Neural Comput.* 29, 2353–2449. <https://doi.org/10.1162/NECO>.
- Rocholz, R., Teussink, M.M., Dolz-Marco, Rosa, Holzhey, C., Dechent, J.F., Tafreshi, Ali-Schulz, S., 2018. SPECTRALIS optical coherence tomography angiography (OCTA): principles and clinical applications. *Heidelb. Eng. Acad.* 1–10.
- Ronneberger, O., Fischer, P., Brox, T., 2015. U-net: Convolutional Networks for Biomedical Image Segmentation. *arXiv* 9351, 234–241. [https://doi.org/10.1007/978-3-319-24574-4\\_28](https://doi.org/10.1007/978-3-319-24574-4_28).
- Rosen, R.B., Andrade Romo, J.S., Krawitz, B.D., Mo, S., Fawzi, A.A., Linderman, R.E., Carroll, J., Pinhas, A., Chui, T.Y.P., 2019. Earliest evidence of preclinical diabetic retinopathy revealed using optical coherence tomography angiography perfused capillary density. *Am. J. Ophthalmol.* 203, 103–115. <https://doi.org/10.1016/j.ajo.2019.01.012>.
- Russakoff, D.B., Lamin, A., Oakley, J.D., Dubis, A.M., Sivaprasad, S., 2019. Deep learning for prediction of AMD progression: a pilot study. *Investig. Ophthalmol. Vis. Sci.* 60, 712–722. <https://doi.org/10.1167/iosv.18-25325>.
- Russel, S.J., Norvig, P., 2020. Artificial Intelligence A Modern Approach, 4th Ed. Prentice Hall.
- Sandhu, H.S., Elmogy, M., Taher Sharafeldeen, A., Elsharkawy, M., El-Adawy, N., Eltanboly, A., Shalaby, A., Keynton, R., El-Baz, A., 2020. Automated diagnosis of diabetic retinopathy using clinical biomarkers, optical coherence tomography, and optical coherence tomography angiography. *Am. J. Ophthalmol.* 216, 201–206. <https://doi.org/10.1016/j.ajo.2020.01.016>.
- Savastano, M.C., Lumbrosio, B., Rispoli, M., 2015. In vivo characterization of retinal vascularization morphology using optical coherence tomography angiography. *Retina* 35, 2196–2203. <https://doi.org/10.1097/IAE.0000000000000635>.
- Schmidt-Erfurth, U., Sadeghipour, A., Gerendas, B.S., Waldstein, S.M., Bogunović, H., 2018. Artificial intelligence in retina. *Prog. Retin. Eye Res.* 67, 1–29. <https://doi.org/10.1016/j.preteyes.2018.07.004>.
- Schottenhamml, J., Moult, E.M., Ploner, S., Lee, B., Novais, E.A., Cole, E., Dang, S., Lu, C. D., Husvogt, L., Waheed, N.K., Duker, J.S., Horngger, J., Fujimoto, J.G., 2016. An automatic, intercapillary area-based algorithm for quantifying diabetes-related capillary dropout using optical coherence tomography angiography. *Retina* 36, S93–S101. <https://doi.org/10.1097/IAE.0000000000001288>.
- Schwartz, D.M., Fingler, J., Kim, D.Y., Zawadzki, R.J., Morse, L.S., Park, S.S., Fraser, S.E., Werner, J.S., 2014. Phase-variance optical coherence tomography: a technique for noninvasive angiography. *Ophthalmology* 121, 180–187. <https://doi.org/10.1016/j.ophtha.2013.09.002>.

- Shahidi, M., Wang, Z., Zelkha, R., 2005. Quantitative thickness measurement of retinal layers imaged by optical coherence tomography. *Am. J. Ophthalmol.* 139 <https://doi.org/10.1016/j.ajo.2005.01.012>.
- Shen, D., Wu, G., Suk, H.-I., 2017. Deep learning in medical image analysis. *Annu. Rev. Biomed. Eng.* 19, 221–248. [https://doi.org/10.1007/978-3-030-33128-3\\_1](https://doi.org/10.1007/978-3-030-33128-3_1).
- Shi, F., Chen, X., Zhao, H., Zhu, W., Xiang, D., Gao, E., Sonka, M., Chen, H., 2015. Automated 3-D retinal layer segmentation of macular optical coherence tomography images with serous pigment epithelial detachments. *IEEE Trans. Med. Imag.* 34, 441–452. <https://doi.org/10.1109/TMI.2014.2359980>.
- Shorten, C., Khoshgoftaar, T.M., 2019. A survey on image data augmentation for deep learning. *J. Big Data* 6. <https://doi.org/10.1186/s40537-019-0197-0>.
- Silver, D., Huang, A., Maddison, C.J., Guez, A., Sifre, L., Van Den Driessche, G., Schrittwieser, J., Antonoglou, I., Panneershelvam, V., Lanctot, M., Dieleman, S., Grewe, D., Nham, J., Kalchbrenner, N., Sutskever, I., Lillicrap, T., Leach, M., Kavukcuoglu, K., Graepel, T., Hassabis, D., 2016. Mastering the game of Go with deep neural networks and tree search. *Nature* 529, 484–489. <https://doi.org/10.1038/nature16961>.
- Son, T., Alam, M., Kim, T.H., Liu, C., Toslak, D., Yao, X., 2019. Highlight article: near infrared oximetry-guided artery–vein classification in optical coherence tomography angiography. *Exp. Biol. Med.* 244, 813–818. <https://doi.org/10.1177/1535370219850791>.
- Spaide, R.F., 2016. Volume-Rendered optical coherence tomography of retinal vein occlusion pilot study. *Am. J. Ophthalmol.* 165, 133–144. <https://doi.org/10.1016/j.ajo.2016.02.037>.
- Spaide, R.F., Kuancklik, J.M., Cooney, M.J., 2015. Retinal vascular layers in macular telangiectasia type 2 imaged by optical coherence tomographic angiography. *JAMA Ophthalmol.* 133, 66–73. <https://doi.org/10.1001/jamaophthalmol.2014.3950>.
- Srinivasan, P.P., Heflin, S.J., Izatt, J.A., Arshavsky, V.Y., Farsiu, S., 2014. Automatic segmentation of up to ten layer boundaries in SD-OCT images of the mouse retina with and without missing layers due to pathology. *Biomed. Opt Express* 5, 348–365. <https://doi.org/10.1364/BOE.5.000348>.
- Sui, X., Zheng, Y., Wei, B., Bi, H., Wu, J., Pan, X., Yin, Y., Zhang, S., 2017. Choroid segmentation from Optical Coherence Tomography with graph-edge weights learned from deep convolutional neural networks. *Neurocomputing* 237, 332–341. <https://doi.org/10.1016/j.neucom.2017.01.023>.
- Sun, J.K., Radwan, S.H., Soliman, A.Z., Lammer, J., Lin, M.M., Prager, S.G., Silva, P.S., Aiello, L.B., Aiello, L.P., 2015. Neural retinal disorganization as a robust marker of visual acuity in current and resolved diabetic macular edema. *Diabetes* 64, 2560–2570. <https://doi.org/10.2337/db14-0782>.
- Sun, Z., Tang, F., Wong, R., Lok, J., Szeto, S.K.H., Chan, J.C.K., Chan, C.K.M., Tham, C.C., Ng, D.S., Cheung, C.Y., 2019. OCT angiography metrics predict progression of diabetic retinopathy and development of diabetic macular edema: a prospective study. *Ophthalmology* 126, 1675–1684. <https://doi.org/10.1016/j.ophtha.2019.06.016>.
- Suykens, J.A.K., Vandewalle, J., 1999. Least squares support vector machine classifiers. *Neural Process. Lett.* 9, 293–300.
- Szkulmowski, M., Grulkowski, I., Szlag, D., Szkulmowska, A., Kowalczyk, A., Wojtkowski, M., 2009. Flow velocity estimation by complex ambiguity free joint Spectral and Time domain Optical Coherence Tomography. *Opt Express* 17, 14281–14297. <https://doi.org/10.1364/OE.17.014281>.
- Szkulmowski, M., Wojtkowski, M., Sikorski, B., Bajraszewski, T., Srinivasan, V.J., Szkulmowska, A., Kalužny, J.J., Fujimoto, J.G., Kowalczyk, A., 2007. Analysis of posterior retinal layers in spectral optical coherence tomography images of the normal retina and retinal pathologies. *J. Biomed. Opt.* 12, 041207. <https://doi.org/10.1117/1.2771569>.
- Tan, B., Wong, A., Bizheva, K., 2018. Enhancement of morphological and vascular features in OCT images using a modified Bayesian residual transform. *Biomed. Opt Express* 9, 2394. <https://doi.org/10.1364/boe.9.002394>.
- Tan, O., Li, G., Lu, A.T.H., Varma, R., Huang, D., 2008. Mapping of macular substructures with optical coherence tomography for glaucoma diagnosis. *Ophthalmology* 115, 949–956. <https://doi.org/10.1016/j.ophtha.2007.08.011>.
- Thakur, B., Kothari, A.R., Chowdhury, S.R., Rajan, J., Girish, G.N., 2018. Segmentation of intra-retinal cysts from optical coherence tomography images using a fully convolutional neural network model. *IEEE J. Biomed. Heal. Informatics* 23, 296–304. <https://doi.org/10.1109/jbhi.2018.2810379>.
- Ting, D.S.W., Pasquale, L.R., Peng, L., Campbell, J.P., Lee, A.Y., Raman, R., Tan, G.S.W., Schmetterer, L., Keane, P.A., Wong, T.Y., 2018. Artificial intelligence and deep learning in ophthalmology. *Br. J. Ophthalmol. bjophthalmol.* <https://doi.org/10.1136/bjophthalmol-2018-313173>, 2018–313173.
- Vermeer, K.A., van der Schoot, J., Lemij, H.G., de Boer, J.F., 2011. Automated segmentation by pixel classification of retinal layers in ophthalmic OCT images. *Biomed. Opt Express* 2, 1743. <https://doi.org/10.1364/boe.2.001743>.
- Vienola, K.V., Braaf, B., Sheehy, C.K., Yang, Q., Tiruveedhula, P., Arathorn, D.W., de Boer, J.F., Roorda, A., 2012. Real-time eye motion compensation for OCT imaging with tracking SLO. *Biomed. Opt Express* 3, 2950. <https://doi.org/10.1364/boe.3.002950>.
- Wang, B., Camino, A., Pi, S., Guo, Y., Wang, J., Huang, D., Hwang, T.S., Jia, Y., 2019. Three-dimensional structural and angiographic evaluation of foveal ischemia in diabetic retinopathy: method and validation. *Biomed. Opt Express* 10, 3522–3532. <https://doi.org/10.1364/boe.10.003522>.
- Wang, H., Rollins, A.M., 2009. Speckle reduction in optical coherence tomography using angular compounding by B-scan Doppler-shift encoding. *J. Biomed. Opt.* 14, 1–7. <https://doi.org/10.1117/1.3155523.Specle>.
- Wang, J., Hormel, T.T., Gao, L., Zang, P., Guo, Y., Wang, X., Bailey, S.T., Jia, Y., 2020a. Automated diagnosis and segmentation of choroidal neovascularization in OCT angiography using deep learning. *Biomed. Opt Express* 11, 927. <https://doi.org/10.1364/boe.379977>.
- Wang, J., Hormel, T.T., You, Q., Guo, Y., Wang, X., Chen, L., Hwang, T.S., Jia, Y., 2020b. Robust non-perfusion area detection in three retinal plexuses using convolutional neural network in OCT angiography. *Biomed. Opt Express* 11, 330–345.
- Wang, J., Zhang, M., Hwang, T.S., Bailey, S.T., Huang, D., Wilson, D.J., Jia, Y., 2017a. Reflectance-based projection-resolved optical coherence tomography angiography [Invited]. *J. Biomed. Opt Express* 8, 1536–1548.
- Wang, Q., Chan, S., Yang, J.Y., You, B., Wang, Y.X., Jonas, J.B., Wei, W. Bin, 2016. Vascular density in retina and choriocapillaris as measured by optical coherence tomography angiography. *Am. J. Ophthalmol.* 168, 95–109. <https://doi.org/10.1016/j.ajo.2016.05.005>.
- Wang, R.K., An, L., 2009. Doppler optical micro-angiography for volumetric imaging of vascular perfusion in vivo. *Opt Express* 17, 8926. <https://doi.org/10.1364/oe.17.008926>.
- Wang, R.K., Jacques, S.L., Ma, Z., Hurst, S., Hanson, S.R., Gruber, A., 2007. Three dimensional optical angiography. *Opt Express* 15, 4083. <https://doi.org/10.1364/oe.15.004083>.
- Wang, Y., Fan, Y., Bhatt, P., Davatzikos, C., 2010. High-dimensional pattern regression using machine learning: from medical images to continuous clinical variables. *NeuroImage* 50, 1519–1535. <https://doi.org/10.1016/j.neuroimage.2009.12.092>.
- Wang, Z., Camino, A., Zhang, M., Wang, J., Hwang, T.S., Wilson, D.J., Huang, D., Li, D., Jia, Y., 2017b. Automated detection of photoreceptor disruption in mild diabetic retinopathy on volumetric optical coherence tomography. *Biomed. Opt Express* 8, 5384–5398. <https://doi.org/10.1364/BOE.8.005384>.
- Wei, X., Camino, A., Pi, S., Cepurna, W., Huang, D., Morrison, J.C., Jia, Y., 2018. Fast and robust standard-deviation-based method for bulk motion compensation in phase-based functional OCT. *Opt. Lett.* 43, 2204–2207. <https://doi.org/10.1364/OL.43.002204>.
- Wei, X., Hormel, T.T., Guo, Y., Hwang, T.S., Jia, Y., 2020a. High-resolution Wide-Field OCT Angiography with a Self-Navigation Method to Correct Microsaccades and Blinks. *vol. 11*, pp. 3234–3245.
- Wei, X., Hormel, T.T., Guo, Y., Hwang, T.S., Jia, Y., 2020b. High-resolution wide-field OCT angiography with a self-navigation method to correct microsaccades and blinks. *Biomed. Opt Express* 11, 3234. <https://doi.org/10.1364/boe.390430>.
- Wei, X., Hormel, T.T., Guo, Y., Jia, Y., 2019. 75-degree Non-mydriatic Single-Volume Optical Coherence Tomographic Angiography, vol. 10, pp. 6286–6295.
- Woetzel, A.K., Lauermann, J.L., Kreitz, K., Alnawaiseh, M., Clemens, C.R., Eter, N., Alten, F., 2019. Optical coherence tomography angiography image quality assessment at varying retinal expertise levels. *J. Curr. Ophthalmol.* 31, 161–167. <https://doi.org/10.1016/j.joco.2018.12.002>.
- Xu, J., Chae, Y., Stenger, B., Datta, A., 2018. Dense bynet: residual dense network for image super resolution. *Proc. - Int. Conf. Image Process. ICIP* 71–75. <https://doi.org/10.1109/ICIP.2018.8451696>.
- Xu, J., Wei, W., Song, S., Qi, X., Wang, R.K., 2016. Scalable wide-field optical coherence tomography-based angiography for in vivo imaging applications. *Biomed. Opt Express* 7, 1905. <https://doi.org/10.1364/boe.7.001905>.
- Yanagi, Y., Mohla, A., Lee, W.K., Lee, S.Y., Mathur, R., Chan, C.M., Yeo, I., Wong, T.Y., Cheung, C.M.G., 2017. Prevalence and risk factors for nonexudative neovascularization in fellow eyes of patients with unilateral age-related macular degeneration and polypoidal choroidal vasculopathy. *Investig. Ophthalmol. Vis. Sci.* 58, 3488–3495. <https://doi.org/10.1167/iovs.16-21167>.
- Yang, J., Yuan, M., Wang, E., Chen, Y., 2019. Comparison of the repeatability of macular vascular density measurements using four optical coherence tomography angiography systems. *J. Ophthalmol.* <https://doi.org/10.1155/2019/4372580>, 2019.
- Yang, Q., Reisman, C.A., Wang, Z., Fukuma, Y., Hangai, M., Yoshimura, N., Tomidokoro, A., Araie, M., Raza, A.S., Hood, D.C., Chan, K., 2010. Automated layer segmentation of macular OCT images using dual-scale gradient information. *Opt Express* 18, 21293–21307. <https://doi.org/10.1364/OE.18.021293>.
- Yu, J.J., Camino, A., Liu, L., Zhang, X., Wang, J., Gao, S.S., Jia, Y., Huang, D., 2019. Signal strength reduction effects in OCT angiography. *Ophthalmol. Retin.* 3, 835–842. <https://doi.org/10.1016/j.joret.2019.04.029>.
- Zang, P., Gao, L., Hormel, T.T., Wang, J., You, Q., Hwang, T.S., Jia, Y., 2020. DcardNet: Diabetic Retinopathy Classification at Multiple Depths Based on Structural and Angiographic Optical Coherence Tomography.
- Zang, P., Gao, S.S., Hwang, T.S., Flaxel, C.J., Wilson, D.J., Morrison, J.C., Huang, D., Li, D., Jia, Y., 2017a. Automated boundary detection of the optic disc and layer segmentation of the peripapillary retina in volumetric structural and angiographic optical coherence tomography. *Biomed. Opt Express* 8, 1306–1318. <https://doi.org/10.1364/BOE.8.001306>.
- Zang, P., Liu, G., Zhang, M., Dongye, C., Wang, J., Pechauer, A.D., Hwang, T.S., Wilson, D.J., Huang, D., Li, D., Jia, Y., 2016. Automated motion correction using parallel-strip registration for wide-field en face OCT angiogram. *Biomed. Opt Express* 7, 2823–2836. <https://doi.org/10.1364/BOE.7.002823>.
- Zang, P., Liu, G., Zhang, M., Wang, J., Hwang, T.S., Wilson, D.J., Huang, D., Li, D., Jia, Y., 2017b. Automated three-dimensional registration and volume rebuilding for wide-field angiographic and structural optical coherence tomography. *J. Biomed. Opt.* 22, 026001. <https://doi.org/10.1117/1.jbo.22.2.026001>.
- Zang, P., Wang, J., Hormel, T.T., Liu, L., Huang, D., Jia, Y., 2019. Automated segmentation of peripapillary retinal boundaries in OCT combining a convolutional neural network and a multi-weights graph search. *Biomed. Opt Express* 10, 4340. <https://doi.org/10.1364/boe.10.004340>.
- Zhang, M., Hwang, T.S., Campbell, J.P., Bailey, S.T., Wilson, D.J., Huang, D., Jia, Y., 2016a. Projection-resolved optical coherence tomographic angiography. *Biomed. Opt Express* 7, 816–828. <https://doi.org/10.1364/BOE.7.000816>.

- Zhang, M., Hwang, T.S., Dongye, C., Wilson, D.J., Huang, D., Jia, Y., 2016b. Automated quantification of nonperfusion in three retinal plexuses using projection-resolved optical coherence tomography angiography in diabetic retinopathy. *Investig. Ophthalmol. Vis. Sci.* 57, 5101–5106. <https://doi.org/10.1167/iovs.16-19776>.
- Zhang, A., Zhang, Q., Wang, R.K., 2015a. Minimizing projection artifacts for accurate presentation of choroidal neovascularization in OCT micro-angiography. *Biomed. Opt Express* 6, 4130–4143. <https://doi.org/10.1364/BOE.6.004130>.
- Zhang, M., Wang, J., Pechauer, A.D., Hwang, T.S., Gao, S.S., Liu, Liang, Liu, Li, Bailey, S. T., Wilson, D.J., Huang, D., Jia, Y., 2015b. Advanced image processing for optical coherence tomographic angiography of macular diseases. *Biomed. Opt Express* 6, 4661. <https://doi.org/10.1364/BOE.6.004661>.
- Zhang, Q., Huang, Y., Zhang, T., Kubach, S., An, L., Laron, M., Sharma, U., Wang, R.K., 2015c. Wide-field imaging of retinal vasculature using optical coherence tomography-based microangiography provided by motion tracking. *J. Biomed. Opt.* 20, 066008 <https://doi.org/10.1117/1.jbo.20.6.066008>.
- Zhang, X., Dastiridou, A., Francis, B.A., Tan, O., Varma, R., Greenfield, D.S., Schuman, J. S., Huang, D., 2017a. Comparison of glaucoma progression detection by optical coherence tomography and visual field. *Am. J. Ophthalmol.* 184, 63–74. <https://doi.org/10.1016/j.ajo.2017.09.020>.
- Zhang, K., Zuo, W., Chen, Y., Meng, D., Zhang, L., 2017b. Beyond a Gaussian denoiser: residual learning of deep CNN for image denoising. *IEEE Trans. Image Process.* 26, 3142–3155. <https://doi.org/10.1109/TIP.2017.2662206>.
- Zhu, J.Y., Park, T., Isola, P., Efros, A.A., 2017. Unpaired image-to-image translation using cycle-consistent adversarial networks. *Proc. IEEE Int. Conf. Comput. Vis. 2017-Octob* 2242–2251. <https://doi.org/10.1109/ICCV.2017.244>.